DRAFT VERSION FEBRUARY 2, 2022
Typeset using LaTeX **twocolumn** style in AASTeX63

Analysis of the spatially-resolved $V-3.6\,\mu$m colors and dust extinction in 257 nearby NGC and IC galaxies

DUHO KIM,[1] ROLF A. JANSEN,[1] ROGIER A. WINDHORST,[1] SETH H. COHEN,[1] TYLER MCCABE,[1]

[1] *School of Earth & Space Exploration, Arizona State University, Tempe, AZ 85287-1404, USA*

(Received January 2, 2019; Revised July 31, 2019; Accepted Aug 1, 2019)

Submitted to ApJ

ABSTRACT

We present and analyze spatially-resolved maps for the observed V- and g-band to 3.6 μm flux ratios and the inferred dust extinction values, A_V, for a sample of 257 nearby NGC and IC galaxies. Flux ratio maps are constructed using PSF-matched mosaics of SDSS g- and r-band images and *Spitzer*/IRAC 3.6 μm mosaics, with all pixels contaminated by foreground stars or background objects masked out. By applying the β_V method (Tamura et al. 2009, 2010), which was recently calibrated as a function of redshift and morphological type by Kim, Jansen, & Windhorst (2017), dust extinction maps were created for each galaxy. The typical 1-σ scatter in β_V around the average, both within a galaxy and in each morphological type bin, is $\sim$20%. Combined, these result in a $\sim$0.4 mag scatter in A_V. β_V becomes insensitive to small-scale variations in stellar populations once resolution elements subtend an angle larger than that of a typical giant molecular cloud ($\sim$200 pc). We find noticeably redder $V-3.6\,\mu$m colors in the center of star-forming galaxies and galaxies with a weak AGN. The derived intrinsic $V-3.6\,\mu$m colors for each Hubble type are generally consistent with the model predictions of Kim et al. (2017). Finally, we discuss the applicability of the β_V dust-correction method to more distant galaxies, for which well-matched *HST* rest-frame visible and *JWST* rest-frame $\sim$3.5μm images will become available in the near-future.

Keywords: (ISM:) dust, extinction — galaxies: photometry — galaxies: stellar populations — galaxies: evolution — surveys — methods: data analysis

1. INTRODUCTION

Cosmic dust between an observer and an astronomical object both absorbs and scatters incoming light (visible and ultraviolet) from the object, and then reradiates the absorbed energy in the far-infrared (FIR) (van de Hulst 1957; Mathis 1990, and references therein). Our rest-frame ultraviolet (UV)–visible view of distant galaxies is therefore modulated by dust extinction. The level of extinction varies across the face of a galaxy and differs from galaxy to galaxy. As a result, our interpretation of the distribution, evolution, and properties of stellar populations within a galaxy is significantly influenced by the intervening dust (e.g., Elmegreen 1980; Kennicutt et al. 2009).

Correcting for dust extinction generally requires either costly (or unattainable) UV to FIR multi-wavelength data in combination with spectral energy distribution (SED) fitting (Conroy 2013, and references therein), or a full radiative transfer analysis (Steinacker et al. 2013, and references therein). In special cases, dust extinction can be corrected in small areas within a galaxy, provided that suitable tracers exist, such as hydrogen recombination lines.

Tamura et al. (2009, hereafter T09) and Tamura et al. (2010, hereafter T10) developed an economical method that offered *approximate* dust-extinction correction called the 'β_V method', $\beta_V = f_V/f_L$, which uses the observed flux ratios of the visible, V-band, and infrared L-band, $\sim$3.5μm, wavelengths. They applied this method to the surface photometry of the nearby, late-type spiral galaxy NGC 959, which unveiled a hidden galactic bar. In order to place the 'β_V method' on a more secure theoretical footing, Kim, Jansen, & Windhorst (2017, hereafter K17) built a library of spectral energy distributions (SEDs) by stacking the SEDs of simple stellar populations (SSPs) —spectral snapshots of a coeval stellar population— for large ensembles of stochastic star-formation histories[1] (SFHs). The SFHs in K17 are designed to reproduce the mean observed SFH as a function of morphological class, assuming open-box metallicity evolution. Furthermore, K17 published both modeler-oriented mass-weighted, and observer-friendly luminosity-weighted predictions, which were then directly compared

Corresponding author: Duho Kim
Duho.Kim@asu.edu

[1] http://lambda.la.asu.edu/betav/

to the luminosity-weighted predictions from integral-field unit (IFU) observations from González Delgado et al. (2015, hereafter GD15) to calibrate the empirical 'β_V method'.

After its long-awaited launch, currently scheduled for 2021, the *James Webb Space Telescope* (*JWST*; Gardner et al. 2006) will observe distant galaxies at near-infrared (NIR; 0.6–5μm) wavelengths with similar spatial resolution as extant visible wavelength images obtained with the *Hubble Space Telescope* (*HST*). Combining rest-frame *JWST* $\sim$3.5μm and rest-frame *HST* V-band observations would extend the 'β_V method' from a redshift of $z \simeq 0$ to redshifts $z \lesssim 2$. With suitably chosen filter pairs and the previously computed intrinsic flux ratios from K17, one could then approximately correct the surface photometry of large samples of galaxies for dust extinction.

In the present paper, we aim to provide a large database of g- and V-band to 3.6 μm flux ratios for local galaxies and their corresponding dust-extinction maps. We will analyze the results of the flux-ratios to evaluate the improvement, fidelity, and robustness offered by the approximate extinction corrections, as well as the nature of exceptional cases. We can then highlight coherent stellar structures previously hidden by dust, in addition to cases where the SED is non-thermal in nature, which can result from (weak) active galactic nuclei (AGN). We also investigate the dependence on the physical resolution of a galaxy by comparing subsets of galaxies at different distances. We then compare our results with those obtained through multi-wavelength SED-fitting found in the literature.

This paper is organized as follows. In §2, we explain how the catalog of sample galaxies was constructed and which data were selected for use. §3 describes the preprocessing of the data, the derivation of the intrinsic β_V-values for each Hubble type, and the creation of the corresponding A_V dust map for each galaxy. In §4.1–2, we illustrate the relationships between β_V-values and various galaxy properties. In §4.3–4, we show the derived radial A_V-profiles for each Hubble type and the hidden coherent features found in the β_V-map. In §5, we discuss the applicability of the β_V-method. We briefly summarize our findings in §6.

We adopt the Planck 2015 (Planck Collaboration et al. 2016) cosmology ($H_0 = 67.8$ km sec^{-1} Mpc^{-1}; $\Omega_m = 0.308$; $\Omega_\Lambda = 0.692$), and we will use AB magnitudes (Oke 1974; Oke & Gunn 1983) throughout.

2. SAMPLE SELECTION AND DATA

We selected our sample galaxies from the Revised New General and Index Catalog[2] (Steinicke 2018; hereafter S18), since it contained data necessary for our analysis of well-studied nearby galaxies. Of the 13,226 objects in the catalog, 9,995 objects are classified as galaxies. Out of these 9,995 galaxies, 568 had available *Spitzer* Enhanced Imaging Product (SEIP) Super Mosaics FITS[3] images, which were observed with the InfraRed Array Camera (IRAC; Fazio et al. 2004) Channel 1 onboard the *Spitzer* Space Telescope (Werner et al. 2004). These observations were taken at a wavelength of 3.6 μm and have a full-width at half maximum (FWHM) resolution of $\sim$1.6″. The galaxies in each mosaic were both well-resolved (size $\gtrsim 100\times$ point spread function; PSF), and roughly centered in the IRAC field-of-view (FOV) (offset from the IRAC pointing center by $\lesssim 1'$). To avoid systematic uncertainties resulting from very large optical depths through a galactic disk, the 568 galaxies were reduced to 410 relatively face-on galaxies with axis-ratio (b/a) larger than 0.5. Column 10 in Table 1 gives for b/a values for individual galaxies. Finally, the 257 galaxies which also had g- and r-band mosaics from the Sloan Digital Sky Survey (SDSS) Data Release (DR) 12 server[4] were selected for the final sample. The SDSS mosaics have average FWHM values of $\sim$1.2″.

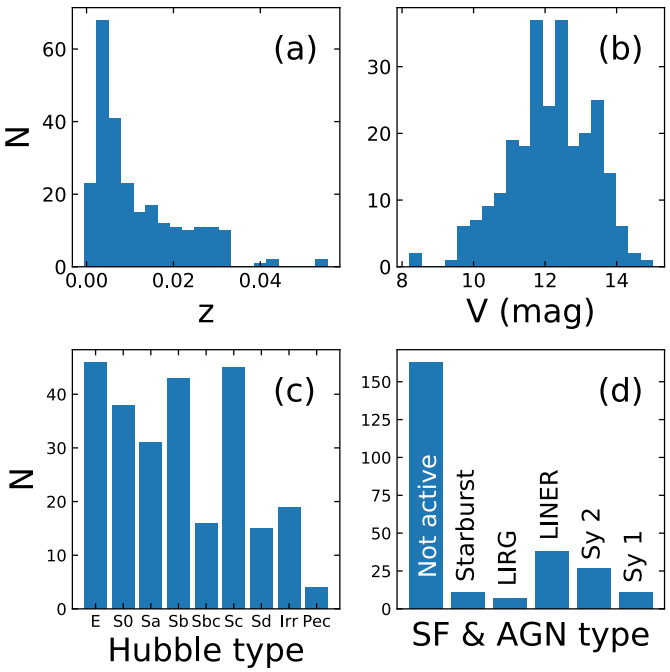

Figure 1. Demographics of the selected 257 NGC/IC sample galaxies containing both *Spitzer*/IRAC 3.6 μm and SDSS g and r mosaics. Distributions detailing the (a) redshifts, (b) V magnitudes, (c) Hubble type, and (d) SF and AGN types are shown for the sample galaxies. See § 2.1 and Table 1 for details.

Figure 1 shows the demographics of the 257 selected galaxies in our sample. The redshift, V-band magnitude, Hubble type, and star formation and/or nuclear activity type were determined from the NASA/IPAC Extragalactic Database[5] (NED), S18, The third Reference Catalogue of Bright Galaxies (de Vaucouleurs et al. 1991,

[2] http://www.klima-luft.de/steinicke/ngcic/ngcic.htm

[3] Flexible Image Transport System (Wells et al. 1981; Hanisch et al. 2001)

[4] https://dr12.sdss.org/mosaics

[5] https://ned.ipac.caltech.edu/

hereafter RC3), and from NED, respectively. The Hubble type was determined from the RC3 numeric T type: E = $T<-3$, S0 = $-3\leq T<0$, Sa = $0\leq T<2$, Sb = $2\leq T<4$, Sbc = $4\leq T<5$, Sc = $5\leq T<7$, Sd = $7\leq T<9$, Irregular = $9\leq T<91$, and Peculiar = $91\leq T<100$. If the 'T-type' from RC3 was missing, the value based on the 'Type' from S18 and the 'Classification' from NED was assigned. These are indicated with asterisks in Column 16 of Table 1. Table 1 also lists the celestial (J2000) coordinates, redshifts, magnitudes (B, V, and 3.6 μm), absolute magnitude (3.6 μm), major-axis size, r-band effective radius, Petrosian half-light radius in V band, position angle of the semi-major axis, Galactic extinction, bulge-to-total light ratio, T-type, T-type uncertainty, SF/AGN classification, and Figure number designation. For the SF and AGN classification, the 'Classification' from NED was used to categorize the galaxies into six types: 'not active', 'Starburst', Luminous InfraRed Galaxy 'LIRG', Low-Ionization Nuclear Emission-line Region 'LINER', 'Seyfert 2', or 'Seyfert 1'. If the NED classification indicates more than one type, we categorize the galaxy with a preference towards later or more active types. For example, NED classifies NGC 0315 as 'LINER', 'Sy3b', and also 'Sy1'. Therefore, we classify NGC 0315 as 'Seyfert 1'. Galaxies without any classification are categorized as 'not active'.

For each of the 257 sample galaxies, the IRAC Channel 1 (3.6 μm) SEIP Cryogenic Release v3.0 Super Mosaics were downloaded from the Spitzer Heritage Archive[6] (SHA). The data products called 'Mean mosaics' were used for the photometry, and those called the 'standard deviation maps' were used for the signal-to-noise ratio (S/N) calculation; following the method detailed in the SEIP Explanatory Supplement[7]. For the V-band data, mosaic images of 257 NGC/IC galaxies were downloaded in both the g and r bands from the SDSS DR12 Science Archive Server[4]. $30'\times30'$ SDSS mosaics with a pixel scale of 0.396″/pixel were selected, such that they had sufficiently larger FOV than the SEIP Super Mosaics. All SDSS images covering the area were used, even if they are not from the *primary*[8] SDSS data set anywhere.

3. ANALYSIS

For each galaxy, the PSFs of the SDSS g- and r-band mosaics were matched to the Spitzer 3.6 μm mosaic. The PyRAF DAOPHOT[9] library was used to build model PSFs. Then, the tasks PSFMATCH[10] and WREGISTER[11] were used to match the SDSS and *Spitzer* PSFs, and then register the image relative to the 3.6 μm *Spitzer* mosaic (see Appendix A for details on the PSF matching). Color composite images in the R, G, and B channels are made from registered IRAC 3.6 μm, the SDSS g-, and r-band mosaics, respectively. These are available in Figure Set 2.[12]

3.1. β_V map and Segmentation

The PSFMATCH task convolves the input image with a convolution kernel to match a PSF of the input image to the corresponding PSF of the reference image (Phillips & Davis 1995):

$$k=\mathscr{F}\left\{\frac{\mathscr{F}(\mathrm{PSF_{ref}})}{\mathscr{F}(\mathrm{PSF_{inp}})}\right\}, \tag{1}$$

where k is the convolution kernel and $\mathscr{F}$ indicates the Fourier transform. After the PSFs were matched and the images were registered, we interpolated the V-band flux between the g- and r-band flux using the transformation formula from Jester et al. (2005) for all stars with $(R\text{-}I)<1.15$ mag:

$$V=g-0.59\times(g-r)-0.01\ [\mathrm{mag}]. \tag{2}$$

The rms residual of this transformation equation is 0.01 mag (Jester et al. 2005). The β_V FITS images were produced by dividing the *pseudo* V-band co-registered FITS images by the 3.6 μm FITS images using the PyRAF task IMARITH[13]. Examples of the resulting images are shown in the top middle panels of Figure Set 2. The β_g images are displayed next to the β_V image in each Figure for comparison.

The host galaxy's regions were selected using the segmentation map generated by SExtractor (Bertin & Arnouts 1996), which was obtained by setting 'CHECKIMAGE_TYPE' as 'SEGMENTATION'. The SExtractor parameters 'DETECT_THRESH', 'BACK_TYPE', 'BACK_SIZE', and 'DETECT_NTHRESH' were carefully controlled to obtain an optimized segmentation map for each galaxy. Foreground stars and background galaxies were selected by visual inspection. Point sources, except the ones in the centers of galaxies, were marked. Extended sources with disparate colors and/or incoherent features were also marked. Their coordinates were recorded manually using the PyRAF DAOEDIT[14] task, so that they could be removed from each segmentation map. For each object removed from the segmentation map, all pixels within a radius of 10 pixels were set to zero. Finally, each segmentation map was individually analyzed and then edited, if necessary, using segeditor (Ryan 2018). The resulting segmentation maps are shown in the lower left panels of Figure Set 2. The cyan region is the galaxy of interest and the gray regions correspond to objects other than the galaxy.

Only the pixels with S/N > 3 in all g-, r-band, and 3.6 μm FITS images were used for further analysis. Each 3.6 μm mosaic comes with an associated standard deviation map,

[6] http://sha.ipac.caltech.edu/applications/Spitzer/SHA/

[7] https://irsa.ipac.caltech.edu/data/SPITZER/Enhanced/SEIP/docs/seip_explanatory_supplement_v3.pdf

[8] https://www.sdss.org/dr12/help/glossary/#surveyprimary

[9] http://stsdas.stsci.edu/cgi-bin/gethelp.cgi?daophot.men

[10] http://stsdas.stsci.edu/cgi-bin/gethelp.cgi?psfmatch

[11] http://stsdas.stsci.edu/cgi-bin/gethelp.cgi?wregister

[12] See the electronic version of this paper for the complete set.

[13] http://stsdas.stsci.edu/cgi-bin/gethelp.cgi?imarith

[14] http://stsdas.stsci.edu/cgi-bin/gethelp.cgi?daoedit

Table 1. The list of NGC/IC galaxy sample

ID	R.A.(J2000)	Decl.(J2000)	z	B	V	3.6μm	3.6μm	a	b/a	$r_{\rm eff}$	$R^P_{50,V}$	PA	Gal. Ext.	B/T	T	eT	Type	SF &	Classification	Figure
	(deg)	(deg)		(mag)	(mag)	(mag)	(Mag)	($'$)		($''$)	($''$)	(deg)	(mag)					AGN		Set 2 #
(1)	(2)	(3)	(4)	(5)	(6)	(7)	(8)	(9)	(10)	(11)	(12)	(13)	(14)	(15)	(16)	(17)	(18)	(19)	(20)	(21)
NGC 0014	2.193333	15.815556	0.002885	12.7	12.1	12.7	–17.8	2.8	0.75	44.4	24.0	25.0	0.117	0.19	10.0	0.3	IBm	0	(R)IB(s)m pec	1
NGC 0023	2.472542	25.923778	0.015231	12.9	12.0	11.5	–22.7	2.1	0.62	14.4	4.2	8.0	0.145	0.49	1.0	0.4	SBa	2	SB(s)a;HII;LIRGSbrst	2
NGC 0193	9.827458	3.331111	0.014723	13.3	12.3	11.7	–22.4	1.4	0.86	19.5	13.8	55.0	0.061	0.78	–2.5	0.6	E/SB0	0	SAB(s)0-:	3
NGC 0266	12.449167	32.277722	0.015547	12.5	11.6	10.3	–23.9	3.0	0.97	42.3	31.2	99.0	0.217	0.28	2.0	0.7	SBab	3	SB(rs)ab LINER	4
NGC 0274	12.757750	–7.056944	0.005837	12.8	11.8	11.7	–20.3	1.5	1.00	*	7.8	25.0	0.211	0.45	–3.0	0.4	E/SB0	0	SAB(r)0- pec	5
NGC 0275	12.767500	–7.066667	0.005817	13.2	12.5	12.3	–19.8	1.5	0.73	*	18.0	126.0	0.211	0.00	6.0	0.4	SBcd/P	0	SB(rs)cd pec	6
NGC 0309	14.177750	–9.913861	0.018886	12.5	11.9	11.8	–22.9	1.94	0.69	44.4	31.2	175.0	0.156	0.06	5.0	0.3	SBc	0	SAB(r)c HII	7
NGC 0315	14.453667	30.352444	0.016485	12.2	11.2	10.3	–24.0	2.08	0.74	36.9	23.4	43.0	0.261	0.78	–4.0	0.5	E2	5	E+:;LINER;Sy3b Sy1	8
NGC 0337	14.958708	–7.577972	0.00549	12.1	11.6	11.0	–21.0	2.9	0.62	31.5	25.8	141.0	0.316	0.31	7.0	0.3	SBcd	0	SB(s)d HII	9
NGC 0382	16.849458	32.403861	0.017442	14.2	13.2	12.3	–22.2	0.7	1.00	*	5.4	*	0.173	0.61	–5.0	0.5	E0	0	E: HII	10
NGC 0383	16.854000	32.412556	0.017005	13.2	12.2	10.8	–23.6	1.6	0.87	*	15.0	30.0	0.173	0.75	–3.0	0.3	E-S0	5	SA0-:;BrClG;Sy LERG	11
NGC 0410	17.745417	33.151889	0.017659	12.5	11.5	11.0	–23.5	2.4	0.54	34.5	16.2	30.0	0.189	0.55	–4.0	0.6	cD	3	E+:;LINER HII	12
NGC 0428	18.232125	0.981556	0.003843	11.9	11.5	12.2	–19.0	4.1	0.76	49.8	34.2	120.0	0.025	0.00	9.0	0.3	SBm	0	SAB(s)m HII	13
NGC 0507	20.916292	33.256056	0.016458	12.2	11.2	10.5	–23.9	3.1	1.00	53.4	37.8	*	0.165	0.39	–2.0	0.3	E-S0	0	SA(r)0^0^;BrClG	14
NGC 0514	21.016250	12.917389	0.008246	12.2	11.7	11.7	–21.1	3.5	0.80	65.7	36.0	110.0	0.073	0.03	5.0	0.3	SBc	0	SAB(rs)c	15
NGC 0596	23.217000	–7.031833	0.006258	11.8	10.9	10.6	–21.7	3.2	0.66	27.3	16.8	40.0	0.107	0.62	–4.0	0.5	E4	0	E+ pec:	16
NGC 0636	24.777208	–7.512611	0.006204	12.4	11.5	11.0	–21.2	2.8	0.75	19.5	10.8	40.0	0.119	0.61	–5.0	0.3	E3	0	E3	17
NGC 0695	27.809333	22.582361	0.032472	13.8	12.8	11.6	–24.2	0.8	0.87	*	6.0	40.0	0.297	0.68	–2.0	1.9	S0/P	2	S0? pec;LIRG HII	18
NGC 0741	29.087625	5.628944	0.018549	12.2	11.1	10.8	–23.8	3.0	0.97	52.2	25.2	90.0	0.133	0.81	–5.0	0.4	E0	0	E0:	19
NGC 0772	29.831583	19.007528	0.008246	11.1	10.3	9.5	–23.4	7.2	0.60	77.1	43.2	130.0	0.157	0.24	3.0	0.3	Sb	0	SA(s)b HII	20
NGC 0777	30.062083	31.429583	0.016728	12.5	11.5	11.0	–23.4	2.5	0.80	34.5	11.4	155.0	0.145	0.66	–5.0	0.3	E1	3	E1 Sy;LINER	21
NGC 0788	30.276875	–6.815528	0.013603	13.0	12.1	11.6	–22.3	1.9	0.74	17.7	12.0	111.0	0.067	0.21	-.0	0.6	S0-a	5	SA(s)0/a:;Sy1 Sy2	22
IC 0195	30.935875	14.709278	0.012168	14.0	13.0	12.7	–21.0	1.17	0.51	*	3.6	126.0	0.137	0.72	–2.0	0.8	S0	0	SAB0^0^	23
IC 0208	32.115583	6.394917	0.011755	14.2	13.4	12.9	–20.7	1.8	1.00	*	19.8	*	0.133	0.03	4.0	0.8	Sbc	0	SAbc	24
IC 0214	33.523292	5.173250	0.030224	14.7	14.2	11.3	–24.4	0.8	0.75	*	3.0	162.0	0.109	0.18	7.0*	*	Sd	2	I? LIRG	25
NGC 0985	38.657375	–8.787611	0.043143	14.0	13.4	12.8	–23.6	1.0	0.90	13.2	8.4	69.0	0.093	0.73	10.0	0.8	Ring/P	5	SBbc? p (Ring) Sy1	26
NGC 0992	39.356208	21.100833	0.013813	13.7	12.8	11.6	–22.3	0.9	0.78	*	5.4	7.0	0.409	0.45	5.0*	*	Sc	2	S? LIRG	27
NGC 1016	39.581500	2.119250	0.022209	12.6	11.6	11.0	–24.0	2.4	1.00	36.0	19.2	*	0.053	0.69	–4.5	0.5	E0	0	E	28
NGC 1143	43.790458	–0.177861	0.028216	14.1	13.1	12.5	–23.0	0.9	0.89	*	8.4	110.0	0.177	0.29	–4.3	0.6	Ring A	0	S0 pec (Ring A)	29
NGC 1144	43.800833	–0.183556	0.028847	13.8	13.0	12.0	–23.6	1.1	0.64	16.8	9.0	130.0	0.177	0.40	3.0*	*	Ring B	4	S pec (Ring B) Sy2	30
NGC 1265	49.565250	41.857750	0.025137	14.4	13.4	11.3	–24.0	1.8	0.89	41.4	12.0	125.0	0.753	0.66	–4.0	0.5	E5	0	E+ LERG	31
NGC 1275	49.950667	41.511694	0.017559	12.6	11.9	10.8	–23.7	2.2	0.77	16.8	22.2	110.0	0.697	0.29	99.0	*	S0/P	4	cD;pec;NLRG;Sy2;LEG	32
NGC 1667	72.154750	–6.319972	0.015167	12.8	12.1	11.4	–22.8	1.8	0.78	18.6	12.6	20.0	0.221	0.05	5.0	0.4	SBc	4	SAB(r)c Sy2	33
NGC 1700	74.234625	–4.865778	0.012972	12.2	11.2	10.5	–23.3	3.3	0.64	18.6	9.0	120.0	0.113	0.82	–5.0	0.3	E4	0	E4	34
NGC 2403	114.214167	65.602556	0.000445	8.9	8.5	8.6	–17.9	21.9	0.56	143.7	126.0	127.0	0.157	0.00	6.0	0.3	SBc	3	SAB(s)cd;HII LINER	35
NGC 2415	114.236208	35.241972	0.012622	12.8	12.4	11.6	–22.2	0.9	1.00	*	7.2	*	0.161	0.37	10.0	1.7	Im	0	Im?	36
IC 0486	120.087417	26.613528	0.026875	14.6	13.7	12.6	–22.8	1.11	0.66	*	6.0	139.0	0.049	0.59	1.0	0.9	SBa	5	Sy1	37
NGC 2500	120.471708	50.737111	0.001681	12.2	11.6	11.1	–18.2	2.9	0.90	*	40.8	48.0	0.129	0.21	7.0	0.3	SBcd	0	SB(rs)d HII	38
NGC 2512	120.782708	23.391833	0.015684	13.9	13.1	12.3	–21.9	1.4	0.64	12.9	11.4	113.0	0.161	0.31	3.0	0.8	SBb	1	SBb Sbrst	39
IC 2239	123.528292	23.866361	0.020174	14.6	13.6	12.9	–21.9	1.3	0.85	*	4.8	168.0	0.185	0.46	0.0*	*	S0	0	S0?	40
NGC 2552	124.835542	50.009639	0.001748	12.6	12.1	13.1	–16.4	3.5	0.66	68.7	43.2	57.0	0.165	0.00	9.0	0.3	SBm	0	SA(s)m?	41

NOTE—Our sample of 257 galaxies, sorted by R.A. Unless stated otherwise, all table entries are taken or derived from NASA/IPAC Extragalactic Database (NED)[a]
Table 1 is published in its entirety in the online journal. A portion is shown here for guidance regarding its form and content.

(1) Same as S18
(2) R.A. in degrees and in epoch J2000.0
(3) Decl. in degrees and in epoch J2000.0
(4) Redshift from NED
(5) Total B-band magnitude from Steinicke 2018
(6) Total V-band magnitude from Steinicke 2018
(7) Total 3.6 μm magnitude measured using GALFIT (AB mag; see Appendix C for more information)
(8) (7) + Distance Modulus from (4): not taking into account K-correction
(9) Major axis in arcminutes
(10) Axis-ratio
(11) Effective radius in r-band in arcseconds from RC3, but recomputed by RAJ from log(Ae) after accounting for the fact that the listed Ae values were diameters, not radii
(12) Petrosian Half-light radius measured in V-band in arcseconds
(13) Position angle from S18 from North through East
(14) Foreground Galactic extinction
(15) Bulge-to-total light ratio measured in 3.6 μm using GALFIT
(16) T-type from RC3 or assigned (with '*') based on (18) and (20)
(17) T-type error from RC3
(18) Morphological type from S18
(19) Assigned SF/AGN classification based on (20) [0 = Not active, 1 = Starburst, 2 = LIRG, 3 = LINER, 4 = Seyfert 2, 5 = Seyfert 1]
(20) Morphological and activity classification from NED
(21) Figure Set number

[a] The NASA/IPAC Extragalactic Database (NED) is operated by the Jet Propulsion Laboratory, California Institute of Technology, under contract with the National Aeronautics and Space Administration.

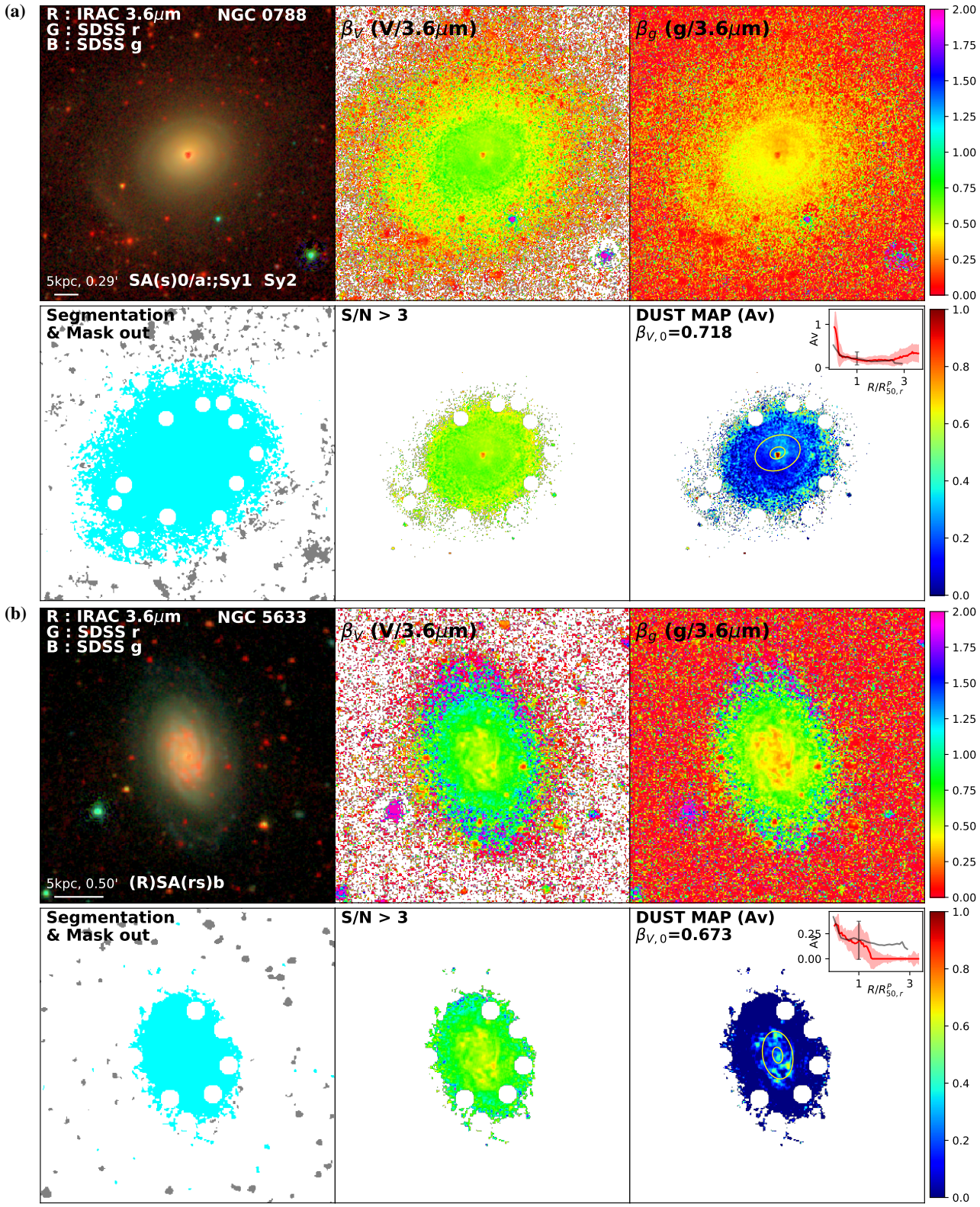

Figure 2. *(a)* NGC 0788 and *(b)* NGC 5633 for each: (top left) RGB color composite from the IRAC 3.6 μm, SDSS r-, and SDSS g-band images, with the classification from the NASA/IPAC Extragalactic Database (NED) on the bottom. (top middle) β_V-image. (top right) β_g-image. (bottom left) SExtractor segmentation map masking out regions near Galactic stars from the galaxy of interest (cyan). (bottom middle) β_V-image of all pixels with a signal-to-noise ratio greater than three in all mosaics for the region defined by the bottom-left segmentation map. (bottom right) Dust A_V-map calculated by the ratio of the β_V to the $\beta_{V,0}$-values (see Equation 3). The A_V-profile (red) is plotted in the top right corner as a function of normalized radius with the GD15 A_V-profile for the corresponding Hubble type (black). The complete figure set (257 images) is temporarily available in Google Drive link before the pulication [b].

[a] https://drive.google.com/open?id=1gN_fUw_RgEG4MOaGg9extOQ_ZbH2lOPo

[b] https://drive.google.com/open?id=1gN_fUw_RgEG4MOaGg9extOQ_ZbH2lOPo

which we used as a noise map. A similar data product is not available for the g- and r-band mosaics, so we measured the standard deviation of the background noise fluctuations and used it as the noise value of each mosaic. The final β_V and A_V maps used for our analysis are shown in the lower middle and right panels of Figure Set 2.

3.2. $\beta_{V,0}$ *derivation*

A β_V-profile of a galaxy was built by taking the median of the β_V-values in elliptical annuli with major axes increasing from 1 pixel to the maximum visible size of a galaxy ('a' in Table 1). This was done with a linear step size of one pixel, while the axis-ratio and position angle (PA) were fixed as 'b/a' and 'PA' in Table 1. The outer ($r > 20\%$ of 'a') annuli with more than half of pixels masked out were excluded from the β_V-profile.

The β_V-profiles were then converted into A_V-profiles using:

$$A_V(r) = 2.5 \times \log\left(\beta_{V,0}/\beta_V(r)\right), \quad (3)$$

where $\beta_{V,0}$ is the global intrinsic β_V-value, assuming negligible extinction at 3.6 μm (see Equation 5 in K17).

The $\beta_{V,0}$-values for each galaxy or Hubble type were derived by grid-searching for the $\beta_{V,0}$-value which had the lowest χ^2 between A_V-profiles from Equation 3 and the average A_V-profiles for each Hubble type from GD15 (see Figure 17 in GD15):

$$\chi^2 = \sum_{r=r0}^{r_n} \frac{(A_V^{\beta_V}(r) - A_V^{GD15}(r))^2}{\sigma^{\beta_V}(r)^2}, \quad (4)$$

where r is the linearly increasing galactic radius normalized by the Petrosian half-light radius (R_{50}^P; Blanton et al. 2001; Yasuda et al. 2001) (see Appendix B for more details), ${A_V}^{\beta_V}(r)$ is the individual or average A_V-profile from Equation 3 for a galaxy or Hubble type respectively, ${A_V}^{\rm GD15}(r)$ is the average A_V-profile for each Hubble type from GD15 for face-on (b/a > 0.63) galaxies, and $\sigma^{\beta_V}(r)$ is the scatter in ${A_V}^{\beta_V}(r)$. We interpolated over ${A_V}^{\beta_V}(r)$, so that the number of radius bins ($r_n = 15$) was the same as in ${A_V}^{\rm GD15}(r)$ within a range of radius of $r = 0$–$3 \times R_{50,V}^P$. For 69 galaxies, the radial steps were less than the FWHM of the matched PSF (1.6″), which indicates that adjacent data points in the ${A_V}^{\beta_V}(r)$ profiles are correlated. However, the $\beta_{V,0}$-values of interest are derived from the statistical average of multiple galaxies per Hubble type. The median β_V-profiles among ≥ 5 galaxies are used in Figures 6 and 7. Medians and 1-σ ranges in the distribution of the resulting β_V-values are shown in Figure 8 and 9. We refer to §4.3 for more details. We also verified that changing the value of r_n from 15 to 30 did not significantly change the $\beta_{V,0}$-values.

3.3. A_V *map using* $\beta_{V,0}$

A_V-maps were generated using Equation 3 as a function of each pixel instead of as a function of radius (see the lower right panels of the Figure Set 2; hereafter 'DUST MAP').

The $\beta_{V,0}$-value for each galaxy was selected as the value with the lowest χ^2 in Equation 4. That $\beta_{V,0}$-value is printed in the top left corner of each 'DUST MAP' panel. The inset in the top right corner of each 'DUST MAP' panel shows ${A_V}^{\beta_V}(r)$ (red) and ${A_V}^{GD15}(r)$ (black) curves as a function of the normalized radius, where the shading represents the 1-σ scatter in the β_V-profile. The errorbar at a radius of $R = R_{50,V}^P$ in the inset represents the uncertainty in the A_V-value at the half-light radius for the corresponding Hubble type from GD15.

Yellow ellipses with major axes values of R_{50}^P and $3 \times R_{50}^P$, corresponding to the tick marks on the A_V-profile plot, are overplotted on each 'DUST MAP' image.

4. RESULTS

4.1. β_V *vs. T-type and* z

The distribution of the β_V-values for our sample galaxies is shown in Figure 3 as a function of T-type. The uncertainty in the T-type and the 1-σ error of the β_V-range are represented by the shape of the ellipses. Furthermore, SF/AGN types are represented by the color of each ellipse. For each integer T-type in our sample, a range of T-types was selected from $\mathrm{T}-0.5 < \mathrm{T} < \mathrm{T}+0.5$. To investigate the trend in this plot, the following steps were taken. For each galaxy in every T-type range, a β_V-value was sampled from a random distribution of β_V-values created using the mean and 1-σ error for each galaxy. This was repeated 1,000 times to determine a more statistically significant average β_V-value for each T-type. In Figure 3, this average is shown by the solid blue line, while the corresponding 1-σ error range is illustrated by the vertical blue lines.

The global β_V-values (solid blue line) in Figure 3 are similar to Figure 14 of K17, which corresponds to the range of β_V-values derived from the K17 SED models that adopted the observational stellar population properties from GD15. From both figures (Figure 3 here and Figure 14 of K17), the average β_V-values, as well as the scatter of the values, increases with T-type. The observed 1-σ scatter in β_V due to both the pixel-to-pixel variations within a galaxy, and from galaxy to galaxy within a Hubble type bin are listed in Table 2. Within individual galaxies, the pixel-to-pixel scatter increases toward later Hubble types, from 0.08 for E to 0.18 for Sb and to 0.33 for Irr&Pec. From galaxy to galaxy, the spread within a Hubble type bin also increases from 0.17 for E through Sbc to 0.45 for Irr&Pec. On average, the spread in β_V around the average, both within a galaxy and for each morphological type bin, are $\sim$20%, which results in a $\sim$0.4 mag scatter in A_V. Slowly evolving old and metal-enriched stellar populations in early-type galaxies tend to be more similar compared to more dynamically evolving young and low-metallicity galaxies of later types, resulting in a wider β_V-range for the latter. However, spiral types with β_V-values less than 0.5 from Brown et al. (2014) in Figure 14 of K17, are not seen in this sample. This difference seems to originate from an intrinsic difference in the type of galaxies from our sample compared to the sample in Brown et al. (2014). Almost all of Brown et al. (2014)'s galaxies have low resolution 5–38μm spectra from the *Spitzer* Infrared Spectrograph (IRS; Houck et al. 2004). This wavelength range is where the

Table 2. The observed 1-σ scatter in β_V, $\beta_{V,0}$, and the calculated 1-σ errors in A_V for galaxies in each Hubble type bin.

	E	S0	Sa	Sb	Sbc	Sc	Sd	Irr&Pec
	(46)[a]	(38)	(31)	(43)	(16)	(45)	(15)	(23)
Within a galaxy[b]	0.08	0.15	0.20	0.18	0.24	0.30	0.31	0.33
From galaxy to galaxy[c]	0.15	0.19	0.16	0.19	0.17	0.27	0.32	0.45
1-σ ranges of $\beta_{V,0}$[d]	0.15	0.25	0.38	0.38	0.35	0.63	0.45	···
$\beta_{V,0}$[e]	$0.55^{+0.08}_{-0.07}$	$0.64^{+0.13}_{-0.12}$	$0.72^{+0.11}_{-0.27}$	$0.68^{+0.19}_{-0.19}$	$0.89^{+0.15}_{-0.20}$	$0.96^{+0.37}_{-0.26}$	$1.14^{+0.29}_{-0.16}$	···
Expected ΔA_V[f]	0.30	0.36	0.36	0.38	0.38	0.45	0.45	0.53

Notes: *(a)* The number of galaxies in each Hubble type bin. *(b)* The mean of 1-σ scatter in the pixel-to-pixel β_V-values within each galaxy (half vertical sizes of the ellipses in Figures 3 and 4) in each Hubble type bin. *(c)* The standard deviation of the galaxy-by-galaxy average β_V-values (central vertical values of the ellipses in Figure 3) in each Hubble type bin. *(d)* The 1-σ scatter of the inferred $\beta_{V,0}$-values for galaxies in each Hubble type bin. See §4.3 and Figure 8 for more details. *(e)* The median and the 1-σ ranges of the inferred $\beta_{V,0}$-values. *(f)* The calculated 1-σ scatters of A_V-values using the derivatives of Equation 3 [$\frac{dA(x)}{dx} = 2.5 \times \frac{d\beta_V(x)/dx}{ln(10)\beta_V(x)}$, where we adopt (d) for $d\beta_V(x)/dx$ and the average β_V-values for each Hubble type bin for β_V(x))].

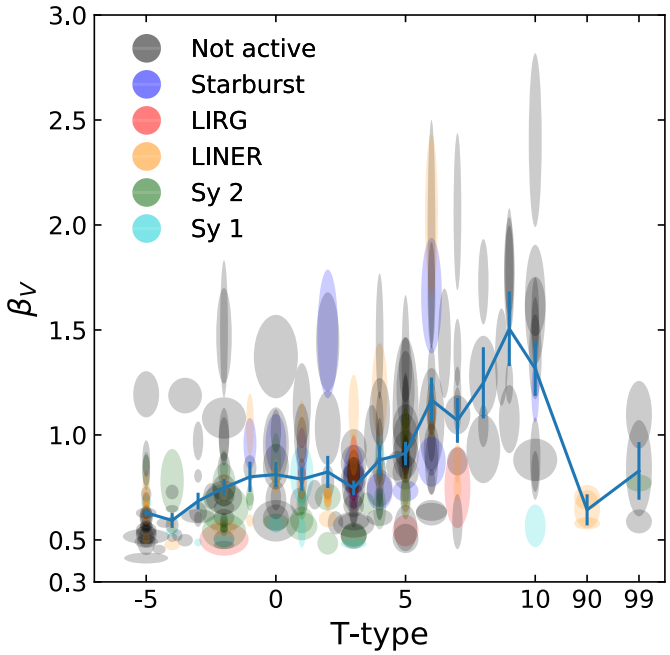

Figure 3. β_V-values as a function of T-type for our sample galaxies. The colors of each ellipse represents the SF/AGN type of each galaxy, while the horizontal and vertical size represents the T-type and the 1-σ β_V uncertainties, respectively. The solid line represents the mean and 1-σ uncertainty for 1000 randomly generated β_V-values for T$-0.5<$T$<$T$+0.5$. No relationship is seen between the SF/AGN types and their β_V-values within each type bin.

re-radiation from dust clouds dominates. Furthermore, these differences can also be attributed to the majority of the galaxies in Brown et al. (2014) being of the SF/AGN class, while the majority of our sample galaxies are listed as 'not active'.

The registered image data has a pixel scale of 0.6″, which is ∼38% of an FWHM of the *Spitzer*/IRAC 3.6 μm mosaics. This corresponds to a galaxy surface area of 13^2, 250^2, 490^2, and 718^2 pc^2 at $z=0.001$, 0.02, 0.04, and 0.06, respectively. Statistically, as redshift increases, the sample surface area increases by factors of ∼370 ($z=0.02$), 1420 ($z=0.04$), and 3050 ($z=0.06$) times compared to a galaxy at a redshift of $z=0.001$. This reduces the scatter of any measurements taken by ∼19, 38, and 55 times compared to the measurement taken at a redshift of $z=0.001$ for a completely random sample. This trend is illustrated in Figure 4, where the median and the scatter in β_V-values decreases significantly as the redshift increases. For redshifts less than $z\lesssim0.02$, this trend holds. This trend can be interpreted as the β_V-values arising from stellar populations not being well-mixed (i.e., being spatially correlated among adjacent pixels), as well as spatial resolution effects, which cause less variance in β_V at $z\gtrsim0.02$.

4.2. *Central β_V vs. SF and AGN activity*

In Figure 3, SF/AGN galaxies are seen to have randomly distributed global β_V-values. However, they do have characteristically lower β_V-values in their centers. Figure 5 shows histograms of the mean β_V-values of the central 3×3 pixels for various SF/AGN galaxies—'Not active', 'LINER', 'Starburst', 'Sy 2', 'Sy 1', and 'LIRG'—from top to bottom in order of decreasing median central β_V-values. Nine galaxies, whose central 3×3 pixels are masked out, are excluded. Central star-forming regions are thought to be enshrouded by molecular clouds, while accretion disks surrounding supermassive black holes are thought to be surrounded by a dust torus (Urry & Padovani 1995). Relatively low β_V-values in the centers of active galaxies support this idea of dusty environments of active SF regions and AGN.

4.3. *$\beta_{V,0}$-values and A_V-profiles*

Figure 6 shows A_V-profiles for each Hubble type, corresponding to the least square fitting of the median-combined β_V-profile to the average A_V-profile from GD15. The $\beta_{V,0}$-values and numbers of galaxies for each Hubble type are also listed. Spiral (Sa, Sb) galaxies have steeper A_V-profiles

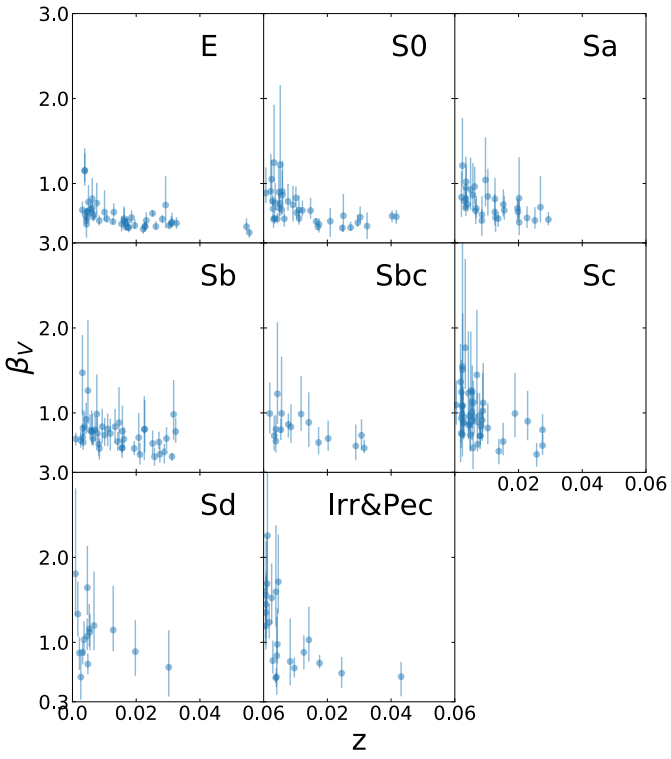

Figure 4. The median and 1-σ range of β_V-values as a function of redshift for each Hubble type in our sample. The scatter in β_V-values for a single galaxy and the width of the distribution for a specific Hubble type decreases as redshift increases, which can be understood as a spatial resolution effect. The trend seems to level out at $z \gtrsim 0.02$, which corresponds to the spatial resolution achieved by *HST* and *JWST* at a redshift of $z \simeq 0.2$.

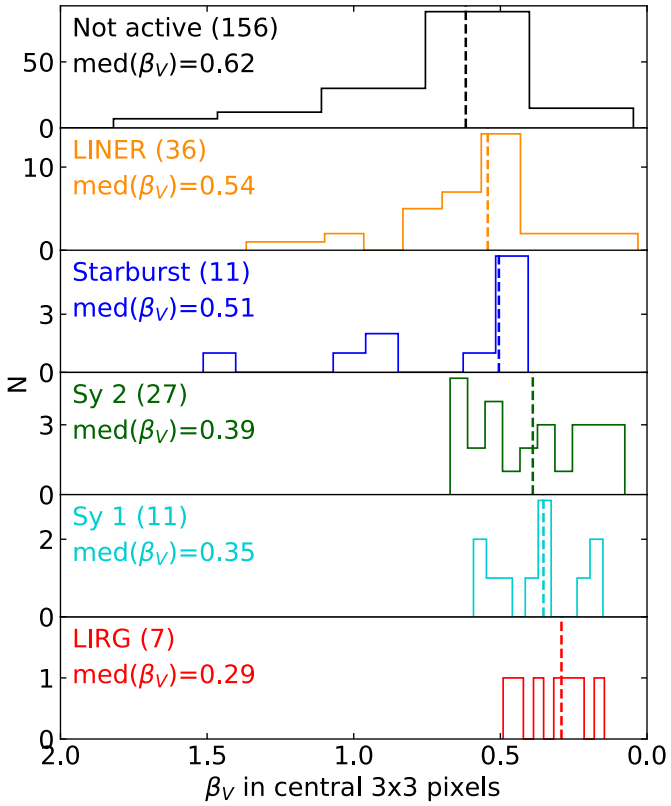

Figure 5. Histograms showing the mean β_V-values for the central 3x3 pixels of each galaxy. From top to bottom, this is done for 248 NGC/IC galaxies with different SF/AGN types: Not active, LINER, Starburst, Seyfert type 2, Seyfert type 1, and LIRG. Compared to average (Not active) galaxies, galaxies with increasing star-formation and/or nuclear activity have decreasing central β_V-values, which implies an increasing amount of dust.

than what was calculated in GD15. Sbc and Sd types show larger stochastic fluctuations, because they have fewer than half of the number of objects compared to other galaxy type bins. The scatter in the β_V-profiles results in larger uncertainties than what was derived from the measurement error at $R = R_{50}^P$ from GD15. This is expected, since the β_V-method uses only two broadband images and a single color $\beta_{V,0}$, whereas GD15 used three-dimensional spectral images and a library of SED models.

The E–Sb types were subgrouped into 'Large bulge' and 'Small bulge' categories by their bulge-to-total light ratios (B/T) derived using GALFIT (Peng et al. 2002, 2010) (see Appendix C for details). The B/T threshold values were arbitrarily chosen, so that there were comparable numbers in each of the two subgroups. The A_V-profile fitting process was then repeated (see Figure 7), which significantly reduced the χ^2 for the small-bulge subgroup of the Sa type. More uniform stellar populations of galaxies in a subgroup result in more reliable A_V-profiles using the β_V-method. This is discussed in § 5.

Figure 8 shows the histograms of the $\beta_{V,0}$-values derived individually for each galaxy. We obtained the $\beta_{V,0}$-values for each galaxy by least square fitting its β_V-profile to the average A_V-profile of the corresponding Hubble type from GD15. The β_V-profile is converted to the A_V-profile with a reference $\beta_{V,0}$-value (see Equation 3). The median and 1-σ ranges are shown as dot-dashed and dotted green vertical lines, while the $\beta_{V,0}$-values derived from the median-combined β_V-profiles are shown as dark brown dashed lines. The median values and associated ranges are listed in Table 2. The 1-σ ranges are comparable to the quadratic sum of the pixel-to-pixel and the galaxy-to-galaxy β_V-variations in Figure 3. The median values derived with these complementary methods agree to within $\pm\,1\,\sigma$.

4.4. *Hidden Coherent Features*

Coherent features buried in a single band or even in composite images (such as top left panel of Figure Set 2) stand out in color images, such as in the β_V, β_g, and/or A_V-maps. The features found in these color maps are detailed in Table 3, along with notes on their corresponding galaxies.

Star-forming regions and dust lanes are the most common features, which have bluer and redder (V-3.6 μm) colors, respectively.

Table 3. Coherent features revealed in the β_V, β_g, and/or A_V images and lists of galaxies containing the features

Features (Number of galaxies)	Galaxies (In the order of ID)
Star-forming regions (15)	**NGC** 14, 337, 2500, 2552, 2730, 3020, 3381, 3395, 3622, 3794, 3870, 3906, 5668, 5669, 5691
Dust lanes (43)	**IC** 676, 1065, 2239, 1551, 2637, **NGC** 23, 266, 275, 1667, 2512, 2608, 2712, 2731, 2742, 2750, 2776, 2782, 2824, 2893, 2906, 3015, 3049, 3055, 3265, 3349, 3351, 3489, 3655, 3720, 3726, 3799, 3801, 3811, 3921, 4194, 5631, 5633, 5992, 7080, 7177, 7479, 7653, 7798
Star-forming regions and dust lanes (30)	**IC** 1076, **NGC** 275, 309, 337, 2403, 2415, 2731, 2742, 2776, 2906, 3020, 3055, 3184, 3192, 3212, 3239, 3310 (pec), 3344, 3370, 3381, 3395 (pec), 3486, 3646, 3659, 3686, 3726, 3794, 3799, 3811, 3870, 4234, 4420, 4449 (Sbrst), 5660, 5691, 5936, 5992, 7714 (pec), 7741, 7753
LIRG-like thick dusty cloud (18)	**IC** 214, 730, 2520 (with blue halo), **NGC** 992, 1144 (pec,Sy2), 3593 (Sy2), 3655, 3683, 3822 (Sy2), 3839, 3934, 4207 (elongated), 4414 (LINER), 5541, 5653, 5953, 5990, 6240
Central dust torus (10)	**IC** 730, 2551, 2637 (Sy1.5), **NGC** 383 (LERG[1]), 3015 (NLAGN[2]), 3349, 3921 (pec), 4014, 4290, 7742 (LINER)
Central dust cloud	**IC** 486 (Sy1), 676, 691, 3050, 5298 (Sy2), **NGC** 788 (Sy1,2), 985 (Sy1), 1275 (cD;pec;NLRG[3]; Sy2;LEG), 2782 (Sy1, Arp 215), 2824 (Sy?), 2831, 3212, 3561, 3720, 3781, 3839 (with blue disk), 3928, 4150, 4162 (AGN), 4194 (pec), 4335, 4369 (intertwined with blue), 4378 (point-like; Sy2), 4412 (LINER), 7177 (LINER), 7674 (Sy2)
Star-forming ring with outer dust ring (1)	**NGC** 3011
Dust ring (2)	**NGC** 2844, 3032
Polar dust ring (2)	**NGC** 2685(Arp 336)[a], 3801
Outer blue ring (3)	**NGC** 3938, 4162, 7217
Dusty disk in E type (1)	**NGC** 3656 (Arp 155, pec, LINER)
Blue disk in E type (2)	**IC** 692, **NGC** 3011
Central blue region (2)	**NGC** 3773 (H II), 7077 (H II)
M82-like outflow (?) (1)	**NGC** 3622
Green center bluer outskirt region (Negative color gradient) (32)	**IC** 208, 2239, 3050, **NGC** 274 (pec), 275 (pec), 309, 428, 2043, 2500, 2604, 2730, 2750, 2776, 2893, 3032, 3049, 3055, 3162, 3319, 3344, 3370, 3489, 3646 (ring), 3659, 3773, 4136, 4234, 4412, 4420, 5584, 5585, 7731
Blue center with green outskirt (3) (Positive color gradient)	**NGC** 3741 (BCD[4]), 4068, 6789

Notes: (1) Low-excitation radio galaxy; (2) Narrow-line AGN; (3) Narrow emission-line radio galaxy; (4) Blue compact dwarf; pec: peculiar, Sbrst: Starburst.

[a] https://apod.nasa.gov/apod/ap140314.html

LIRG-like galaxies are dominated by optically-thick dust clouds that are likely to be undergoing cold gas accretion from the cosmic web, harboring an AGN (see Müller-Sánchez et al. 2018; Saito et al. 2018, for e.g., the case of NGC 6240), or experiencing the aftermath of a recent merger (see Pingel et al. 2018, for e.g., the case of NGC 4414).

AGN appear to have at least local dust clouds such as NGC 1275 (Tanada et al. 2018) and NGC 985 (Appleton & Marcum 1993), except the active, dustless, bulgeless, intermediate-mass black hole in NGC 3319 (see Jiang et al. 2018).

Inner and outer rings in NGC 3011 have been found by Gil de Paz et al. (2003). The inner ring could have been produced by a starburst-driven shock interacting with the surrounding medium (Marino et al. 2013).

Dust rings in NGC 2844 and NGC 3032 are also found and included in the Atlas of Resonance Rings As Known In S^{4}G (ARRAKIS; Comerón et al. 2014). These rings appear to be formed by a dynamical resonance resulting from non-axisymmetries in galaxy disks (Comerón et al. 2014).

NGC 2685 (Arp 336, also known as "The Helix Galaxy") is a well-known polar ring galaxy (Sandage 1961; Eskridge & Pogge 1997), which has an outer ring perpendicular to the galactic disk. This is seemingly the remains of a merger with a polar-orbiting smaller galaxy.

NGC 3801 could be at an earlier stage of an NGC 2685-like merger (Hota et al. 2012). The merging event ∼2–3 Gyr ago is presumably responsible for nuclear-ring in NGC 7742 (Martinsson et al. 2018), while the minor merger ∼200 Myr ago (Knierman et al. 2012, 2013) is responsible for the central dust in NGC 2782 and in NGC 4194 (König et al. 2018).

Balcells (1997) argues that the dusty disk, two tidal tails, and shells in E-type NGC 3656 is the outcome of a disk-disk major merger. Conversely, the blue disk in the E-type, but low-mass, "blue sequence" galaxy IC 692 is from cold-mode gas accretion (Moffett et al. 2012).

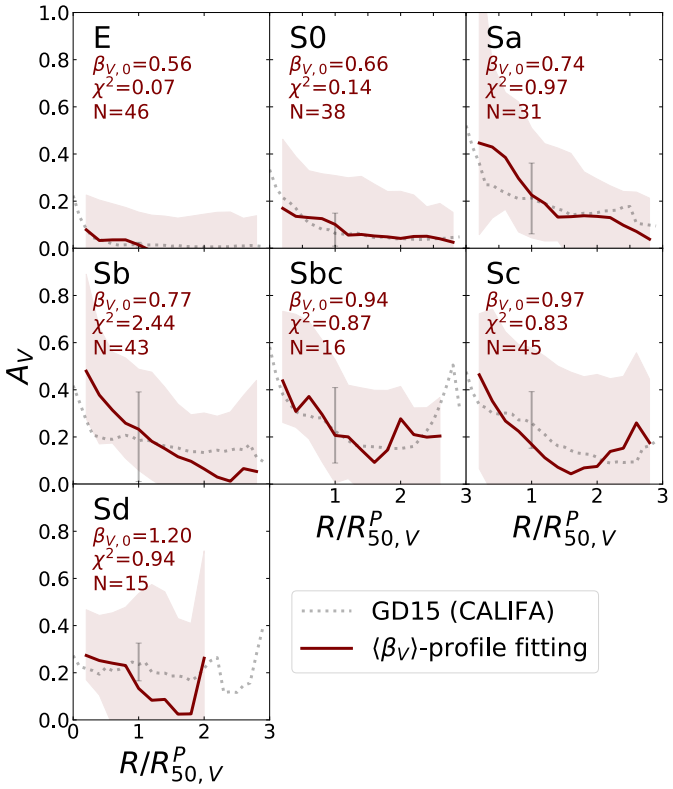

Figure 6. A_V-profiles as a function of galactic radius normalized by the Petrosian half-light radius for different Hubble types. The gray dotted lines are the averaged A_V-profiles of face-on (b/a >0.63) galaxies as a function of Hubble type from the CALIFA survey of González Delgado et al. (2015). The error bars at a radius of $R = R^P_{50}$ indicate the measurement errors at the half-light radii for each Hubble type from GD15 (see their Fig. 14), while the solid, dark brown lines are A_V-profiles generated from Equation 3 using the median β_V-profile for each Hubble type. The $\beta_{V,0}$-value with the smallest χ^2 in Equation 4 is grid-searched, and the results are detailed on each panel along with the number of galaxies for each type. The light purple shaded regions represent the 1-σ ranges of the β_V-profiles. Sections of the A_V-profiles where the number of available β_V-profiles less than five are excluded from the χ^2 fitting. This is the case for the outskirts of the Sd types. Overall, the profiles agree with the CALIFA survey results from GD15. Slight deviations are seen in the slopes of spiral galaxies (Sa, Sb) and in the stochastic fluctuations of galaxies with small sample sizes (Sbc, Sd).

Both NGC 3773 and NGC 7077 have central blue features that are classified as H II regions, which are probably caused by Wolf-Rayet stars (Miralles-Caballero et al. 2016).

The sandglass-shaped feature in NGC 3622, which resembles the outflow of M82, has never been reported. SDSS DR12 classifies this galaxy as a starburst galaxy, which reinforces the idea of an outflow-like feature. Strong Hα and

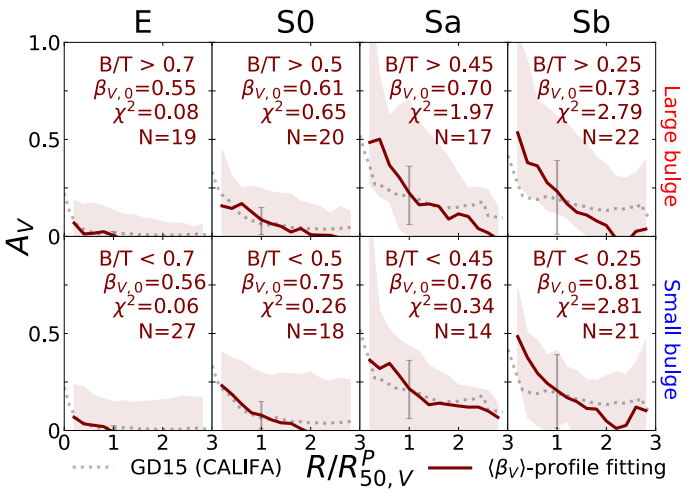

Figure 7. Same as Figure 6, but with each Hubble type divided into large and small bulge subgroups. The subgroups are defined by bulge-to-total light ratios larger or smaller than 0.7, 0.5, 0.45, and 0.25 for the E, S0, Sa, and Sb types, respectively. A_V-profiles for Sa type galaxies are in closer agreement for the small-bulge subgroup, which is a direct result of a more uniform stellar population within that subgroup.

O III emission lines might be the cause of this particular feature[15].

In total, 32 galaxies have noticeable negative color gradients, while 3 have positive color gradients. The color gradients of NUV(*Galaxy Evolution Explorer (GALEX)*) / 3.6 μm (S^{4}G) observations for the disks of 1931 nearby galaxies ($z < 0.01$) also show negative color gradients (see Figure 6 in Bouquin et al. 2018, see also de Jong 1996, Taylor et al. 2005, Kim & Im 2013). These color gradients are in agreement with the global scenario of inside-out formation of disks.

5. DISCUSSION

In this study of 257 NGC/IC galaxies at a redshift of $z \simeq 0$, we find that:

1) *Early-type galaxies have lower and narrower ranges of β_V and $\beta_{V,0}$-values than later type galaxies* (see Figures 3 and 8). This trend can be explained by an increased amount of old stellar populations with quenched star-formation in early-type galaxies.

2) *Spiral galaxies have steeper A_V-profiles.* The A_V-profiles for Sa galaxies with small bulges agree better with what was published in GD15 than for the ones with large bulges. The steeper A_V-profile slopes are the result of the red-bulge population in their galaxy centers, which increases the inferred extinction values. Before using the β_V-method for spiral galaxies with

[15] http://skyserver.sdss.org/dr12/en/tools/explore/Summary.aspx?id=1237651273508651034

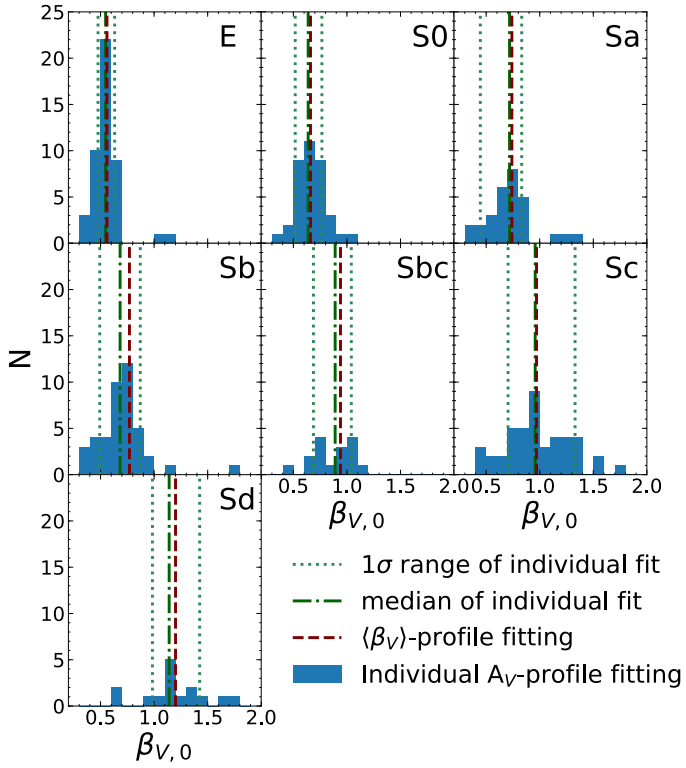

Figure 8. Histograms of the $\beta_{V,0}$-values corresponding to the least square fitting of the A_V-profiles of each galaxy to the average A_V-profile of each Hubble type from GD15. The green dot-dashed and dotted lines represent the median and 1-σ ranges, respectively. The brown dashed lines show the least square fitting result of median-combined β_V-profiles for each Hubble type (see Figure 6).

large bulges, these larger gradients need to be taken into account.

3) *The K17 model holds for nearby galaxies.* K17 published the intrinsic flux ratios of various visible – near-infrared filters ($\beta_{\lambda,0}$) with respect to the L filter ($\sim$3.5μm) as a function of redshift for galaxies having SFHs characteristic of early-types (E and S0), spirals (Sa–Sbc), and late-types (Sbc–Sd). K17 approximated metallicity evolution by stacking the SEDs of simple stellar populations as a function of SFH, which is different for each SFH type (see Appendix D for details). Figure 9 shows the $\beta_{V,0}$-values at a redshift of $z\simeq0$ from the K17 model, as well as the observed data from the current study. The K17 model values are indicated by colored lines for early-types, spirals, and late-types with metallicity offsets: $Z(z{=}0)=2.5$, 1.0, and 0.4 $Z_\odot$ from bottom to top. K17 selected the metallicity offset values arbitrarily, matching the metallicities of empirical SED model of SSP. Metallitiy offsets result in mass-weighted metallicities, $\langle Z\rangle_m$ at $z=0$, as indicated above or below each line (see Figure 12). The gray dotted lines are $\beta_{V,0}$-values without any metallicity evolution taken into account. The

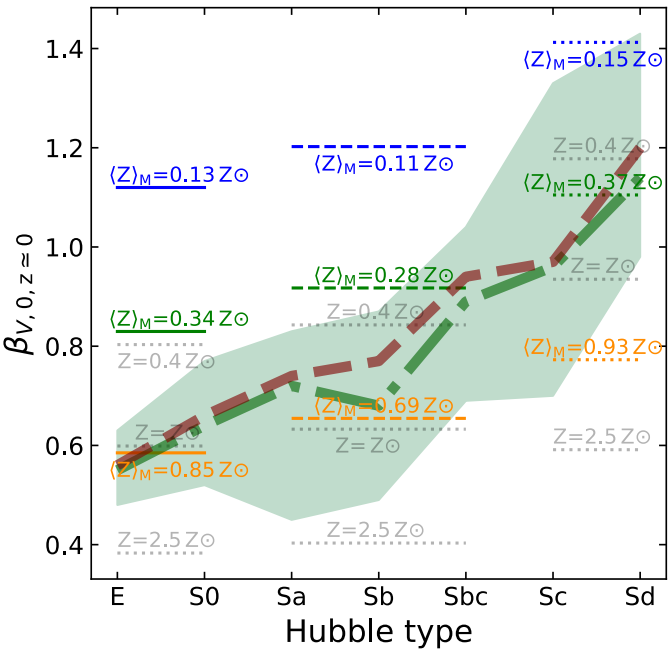

Figure 9. $\beta_{V,0}$-values at $z\simeq0$ for galaxies of Hubble type E–Sd. The green dot-dashed line and shaded region indicate the median and 1-σ limits of the $\beta_{V,0}$-values for galaxies in each Hubble type bin (see Figure 8). The thick brown dashed line indicates the $\beta_{V,0}$ values derived from the median combined ⟨β_V⟩-profiles for each Hubble type. Horizontal lines show the expected model values from K17, where the colors and line styles correspond to those from Figure 12 (see Appendix D). Mass-weighted metallicities for models at a redshift of $z=0$ are shown above or below each line. $\beta_{V,0}$-values with no metallicity evolution are plotted as light gray dotted lines. Mass-weighted metallicity ranges for each Hubble type from GD15 (see their Fig.11) match well to the mass-weighted metallicity range, where $\beta_{V,0}$-values are distributed throughout the green shaded region.

$\beta_{V,0}$-values derived in this study through A_V-profile matching are plotted on top of the horizontal lines from K17. The thick green dashed line and the corresponding green shaded region represent the median and 1-σ ranges of the $\beta_{V,0}$-values derived from the β_V-profiles of individual galaxies in each Hubble type bin, respectively (see Figure 8). The thick brown dashed line shows the $\beta_{V,0}$-values derived from the average β_V-profile of all galaxies in each Hubble type bin. The $\beta_{V,0}$-values fall within a range of observed $\langle Z\rangle_m$ from GD15 of $1.3^{+0.7}_{-0.5}$, $1.2^{+0.6}_{-0.4}$, $0.9^{+0.5}_{-0.4}$, $0.8^{+0.4}_{-0.3}$, $0.6^{+0.4}_{-0.2}$, $0.4^{+0.3}_{-0.2}$, and $0.3^{+0.3}_{-0.1}$ $Z\odot$ for the E, S0, Sa, Sb, Sbc, Sc, and Sd types, respectively (see Figure 11 of GD15).

The $\beta_{V,0}$-values from the K17 model were confirmed by matching the $\beta_{V,0}$-values at a redshift of $z\simeq0$ to the observations. K17 derived $\beta_{V,0}$-values using empirical models that were developed based upon observations of galaxies including a sample at redshifts $z\gtrsim2$. The K17 model at a redshift

of $z \simeq 0$ is the end-product of an accumulation of SEDs of simple stellar populations as a function of SFH and metallicity evolution. Any discrepancy at the intermediate redshift would have resulted in the mismatch at redshift $z \simeq 0$. Therefore, with *HST* and future *JWST* data, we expect the β_V-method would work for galaxies at a redshift $z \lesssim 2$ with a careful classification of galaxy morphology and metallicities.

JWST/NIRCam's images are Nyquist sampled at 4 μm with 0.0647″ pixels in the long wavelength arm (Beichman et al. 2012). That scale corresponds to 123, 220, and 406 pc at redshifts of $z = 0.1$, 0.2, and 0.5, respectively. NIRCam's pixel scale corresponds to a physical scale larger than ∼200 pc at redshift $z \gtrsim 0.2$. The same galaxies at these redshifts observed with both *HST* and *JWST* would look similar to galaxies observed at a redshift of $z = 0.02$ by *Spitzer* at IRAC's 3.6 μm resolution, such as NGC 1016, IC 2239, NGC 2832, NGC 2892, and NGC 2937 from our sample (see the last paragraph of § 4.1). The spatial resolution effects from using the β_V method in an *HST* and *JWST* galaxy survey would therefore not be significant over the redshift range $0.2 < z < 2.0$. For comparison, these spatial resolution effects were evident in the *Spitzer* observations in our sample at a redshift of $z < 0.02$. As a result of the increased resolution of *HST* and *JWST*, regions smaller than giant molecular clouds would be resolved at redshifts of $z < 0.2$ (Murray 2011, $\lesssim$200 pc). Therefore the β_V-method using the average color over multiple stellar populations would become less effective at these redshifts.

In addition to dust correction via the β_V-map, the β_V-method may also serve as a detection tool for AGN and bluer/redder coherent features. Since AGN are typically surrounded by thick dust tori, central β_V-values lower than the rest of the galaxy could serve as an indication of AGN activity. This method was able to find previously known features, such as resonance rings and H II regions, and also an outflow-like feature that has not been observed before.

6. SUMMARY

Studying PSF-matched images of 257 NGC/IC galaxy mosaics in the SDSS g and r filters and *Spitzer* 3.6 μm mosaics, we conclude the following:

1) The $\beta_{V,0}$-values derived from A_V-profile matching with the IFU-SED fitting results agree with the models from K17 to within the stated errors.

2) β_V becomes insensitive to small-scale variations in stellar populations once resolution elements subtend an angle larger than that of a typical giant molecular cloud (∼200 pc). At the resolution of our images this corresponds to a redshift $z \gtrsim 0.02$; when combining *HST* and *JWST* images the method should be robust for $z \gtrsim 0.2$.

3) SF/AGN galaxies have lower β_V-values in the central regions.

We conclude that the β_V-method can serve as a simple dust correction method for large galaxy surveys in the redshift range $0.2 < z < 2$, where *JWST* observations will sample rest-frame ∼3.5 μm, and *HST* observations sample rest-frame visible wavelengths. This will become particularly useful when no, or only a limited number of, other broadband images are available.

Acknowledgements: This work is funded by NASA/ADAP grant NNX12AE47G (PI: R. A. Jansen). RAW acknowledges support from NASA JWST grants NAG5-12460, NNX14AN10G, and 80NSSC18K0200. We thank Rosa M. González Delgado and Rubén García-Benito for sending us the data of the plots in their paper (GD15). DK thanks Wolfgang Steinicke for his permission to use his Revised NGC and IC catalog. DK thanks Russell Ryan for sharing the IDL code segeditor (Ryan 2018), which was very helpful for editing SEXTRACTOR segmentation maps. We appreciate the anonymous referee who provided constructive comments and insights. We thank Bhavin Joshi, Teresa Ashcraft, and Brent Smith for helpful discussion and comments. We thank Tom Tyburczy and Garrett Rand for their help with coding PSF Extraction and documenting the procedure. We thank Gabriela Huckabee for reviewing the draft of this paper and giving helpful comments.

This work is based on observations made with the *Spitzer* Space Telescope, which is operated by the Jet Propulsion Laboratory, California Institute of Technology under a contract with NASA. SEIP are provided by The *Spitzer*Science Center (SSC) and the Infrared Science Archive (IRSA).

Funding for the Sloan Digital Sky Survey IV has been provided by the Alfred P. Sloan Foundation, the U.S. Department of Energy Office of Science, and the Participating Institutions. SDSS-IV acknowledges support and resources from the Center for High-Performance Computing at the University of Utah. The SDSS web site is www.sdss.org.

SDSS-IV is managed by the Astrophysical Research Consortium for the Participating Institutions of the SDSS Collaboration including the Brazilian Participation Group, the Carnegie Institution for Science, Carnegie Mellon University, the Chilean Participation Group, the French Participation Group, Harvard-Smithsonian Center for Astrophysics, Instituto de Astrofísica de Canarias, The Johns Hopkins University, Kavli Institute for the Physics and Mathematics of the Universe (IPMU) / University of Tokyo, the Korean Participation Group, Lawrence Berkeley National Laboratory, Leibniz Institut für Astrophysik Potsdam (AIP), Max-Planck-Institut für Astronomie (MPIA Heidelberg), Max-Planck-Institut für Astrophysik (MPA Garching), Max-Planck-Institut für Extraterrestrische Physik (MPE), National Astronomical Observatories of China, New Mexico State University, New York University, University of Notre Dame, Observatário Nacional / MCTI, The Ohio State University, Pennsylvania State University, Shanghai Astronomical Observatory, United Kingdom Participation Group, Universidad

Nacional Autónoma de México, University of Arizona, University of Colorado Boulder, University of Oxford, University of Portsmouth, University of Utah, University of Virginia, University of Washington, University of Wisconsin, Vanderbilt University, and Yale University.

This research has made use of the NASA/IPAC Extragalactic Database (NED), which is operated by the Jet Propulsion Laboratory, California Institute of Technology, under contract with the National Aeronautics and Space Administration.

PyRAF is a product of the Space Telescope Science Institute, which is operated by AURA for NASA.

Facilities: IRSA, NED, Sloan, Spitzer

Software: Python, Numpy, Scipy, PyRAF, Astropy, IRAF, DS9, GALFIT, IDL, SExtractor; segeditor IDL code written by Russell Ryan.

REFERENCES

Appleton, P. N., & Marcum, P. M. 1993, ApJ, 417, 90, doi: 10.1086/173293

Balcells, M. 1997, ApJL, 486, L87, doi: 10.1086/310854

Behroozi, P. S., Wechsler, R. H., & Conroy, C. 2013, ApJ, 770, 57, doi: 10.1088/0004-637X/770/1/57

Beichman, C. A., Rieke, M., Eisenstein, D., et al. 2012, Science opportunities with the near-IR camera (NIRCam) on the James Webb Space Telescope (JWST), doi: 10.1117/12.925447

Bertin, E., & Arnouts, S. 1996, A&AS, 117, 393, doi: 10.1051/aas:1996164

Blanton, M. R., Dalcanton, J., Eisenstein, D., et al. 2001, AJ, 121, 2358, doi: 10.1086/320405

Bouquin, A. Y. K., Gil de Paz, A., Muñoz-Mateos, J. C., et al. 2018, ApJS, 234, 18, doi: 10.3847/1538-4365/aaa384

Brown, M. J. I., Moustakas, J., Smith, J.-D. T., et al. 2014, ApJS, 212, 18, doi: 10.1088/0067-0049/212/2/18

Bruzual, G., & Charlot, S. 2003, MNRAS, 344, 1000, doi: 10.1046/j.1365-8711.2003.06897.x

Comerón, S., Salo, H., Laurikainen, E., et al. 2014, A&A, 562, A121, doi: 10.1051/0004-6361/201321633

Conroy, C. 2013, Annual Review of Astronomy and Astrophysics, 51, 393, doi: 10.1146/annurev-astro-082812-141017

de Jong, R. S. 1996, A&A, 313, 377

de Vaucouleurs, G., de Vaucouleurs, A., Corwin, Jr., H. G., et al. 1991, Third Reference Catalogue of Bright Galaxies. Volume I: Explanations and references. Volume II: Data for galaxies between 0^h and 12^h. Volume III: Data for galaxies between 12^h and 24^h. (P.. Springer, New York, NY (USA))

Elmegreen, D. M. 1980, ApJS, 43, 37, doi: 10.1086/190666

Eskridge, P. B., & Pogge, R. W. 1997, ApJ, 486, 259, doi: 10.1086/304517

Fazio, G. G., Hora, J. L., Allen, L. E., et al. 2004, ApJS, 154, 10, doi: 10.1086/422843

Gardner, J. P., Mather, J. C., Clampin, M., et al. 2006, SSRv, 123, 485, doi: 10.1007/s11214-006-8315-7

Gil de Paz, A., Madore, B. F., Noeske, K., et al. 2003, ApJ, 596, L179, doi: 10.1086/379601

González Delgado, R. M., Pérez, E., Cid Fernandes, R., et al. 2014, A&A, 562, A47, doi: 10.1051/0004-6361/201322011

González Delgado, R. M., García-Benito, R., Pérez, E., et al. 2015, A&A, 581, A103, doi: 10.1051/0004-6361/201525938

Hanisch, R. J., Farris, A., Greisen, E. W., et al. 2001, A&A, 376, 359, doi: 10.1051/0004-6361:20010923

Hota, A., Rey, S.-C., Kang, Y., et al. 2012, MNRAS, 422, L38, doi: 10.1111/j.1745-3933.2012.01231.x

Houck, J. R., Roellig, T. L., van Cleve, J., et al. 2004, ApJS, 154, 18, doi: 10.1086/423134

Jester, S., Schneider, D. P., Richards, G. T., et al. 2005, AJ, 130, 873, doi: 10.1086/432466

Jiang, N., Wang, T., Zhou, H., et al. 2018, ArXiv e-prints. https://arxiv.org/abs/1810.10283

Kennicutt, Jr., R. C., Hao, C.-N., Calzetti, D., et al. 2009, ApJ, 703, 1672, doi: 10.1088/0004-637X/703/2/1672

Kim, D., & Im, M. 2013, ApJ, 766, 109, doi: 10.1088/0004-637X/766/2/109

Kim, D., Jansen, R. A., & Windhorst, R. A. 2017, ApJ, 840, 28, doi: 10.3847/1538-4357/aa6ba1

Knierman, K., Knezek, P. M., Scowen, P., Jansen, R. A., & Wehner, E. 2012, ApJL, 749, L1, doi: 10.1088/2041-8205/749/1/L1

Knierman, K. A., Scowen, P., Veach, T., et al. 2013, ApJ, 774, 125, doi: 10.1088/0004-637X/774/2/125

König, S., Aalto, S., Muller, S., et al. 2018, A&A, 615, A122, doi: 10.1051/0004-6361/201732436

Leitherer, C., Schaerer, D., Goldader, J. D., et al. 1999, ApJS, 123, 3, doi: 10.1086/313233

Maiolino, R., & Mannucci, F. 2018, ArXiv e-prints. https://arxiv.org/abs/1811.09642

Maiolino, R., Nagao, T., Grazian, A., et al. 2008, A&A, 488, 463, doi: 10.1051/0004-6361:200809678

Marino, A., Plana, H., Rampazzo, R., et al. 2013, MNRAS, 428, 476, doi: 10.1093/mnras/sts039

Martinsson, T. P. K., Sarzi, M., Knapen, J. H., et al. 2018, A&A, 612, A66, doi: 10.1051/0004-6361/201730955

Mathis, J. S. 1990, Annual Review of Astronomy and Astrophysics, 28, 37, doi: 10.1146/annurev.aa.28.090190.000345

Miralles-Caballero, D., Díaz, A. I., López-Sánchez, Á. R., et al. 2016, A&A, 592, A105, doi: 10.1051/0004-6361/201527179

Moffett, A. J., Kannappan, S. J., Baker, A. J., & Laine, S. 2012, ApJ, 745, 34, doi: 10.1088/0004-637X/745/1/34

Müller-Sánchez, F., Nevin, R., Comerford, J. M., et al. 2018, Nature, 556, 345, doi: 10.1038/s41586-018-0033-2

Murray, N. 2011, ApJ, 729, 133, doi: 10.1088/0004-637X/729/2/133

Oke, J. B. 1974, ApJS, 27, 21, doi: 10.1086/190287

Oke, J. B., & Gunn, J. E. 1983, ApJ, 266, 713, doi: 10.1086/160817

Peng, C. Y., Ho, L. C., Impey, C. D., & Rix, H.-W. 2002, AJ, 124, 266, doi: 10.1086/340952

—. 2010, AJ, 139, 2097, doi: 10.1088/0004-6256/139/6/2097

Phillips, A. C., & Davis, L. E. 1995, in Astronomical Society of the Pacific Conference Series, Vol. 77, Astronomical Data Analysis Software and Systems IV, ed. R. A. Shaw, H. E. Payne, & J. J. E. Hayes, 297

Pingel, N. M., Pisano, D. J., Heald, G., et al. 2018, ApJ, 865, 36, doi: 10.3847/1538-4357/aad816

Planck Collaboration, Ade, P. A. R., Aghanim, N., et al. 2016, A&A, 594, A13, doi: 10.1051/0004-6361/201525830

Ryan, Jr, R. E. 2018, ArXiv e-prints. https://arxiv.org/abs/1808.04378

Saito, T., Iono, D., Ueda, J., et al. 2018, MNRAS, 475, L52, doi: 10.1093/mnrasl/slx207

Sandage, A. 1961, The Hubble Atlas of Galaxies (Washington: Carnegie Institution)

Steinacker, J., Baes, M., & Gordon, K. D. 2013, Annual Review of Astronomy and Astrophysics, 51, 63, doi: 10.1146/annurev-astro-082812-141042

Stetson, P. B. 1987, PASP, 99, 191, doi: 10.1086/131977

Tamura, K., Jansen, R. A., Eskridge, P. B., Cohen, S. H., & Windhorst, R. A. 2010, AJ, 139, 2557, doi: 10.1088/0004-6256/139/6/2557

Tamura, K., Jansen, R. A., & Windhorst, R. A. 2009, AJ, 138, 1634, doi: 10.1088/0004-6256/138/6/1634

Tanada, K., Kataoka, J., Arimoto, M., et al. 2018, ApJ, 860, 74, doi: 10.3847/1538-4357/aac26b

Taylor, V. A., Jansen, R. A., Windhorst, R. A., Odewahn, S. C., & Hibbard, J. E. 2005, ApJ, 630, 784, doi: 10.1086/432028

Urry, C. M., & Padovani, P. 1995, PASP, 107, 803, doi: 10.1086/133630

van de Hulst, H. C. 1957, Light Scattering by Small Particles (New York: John Wiley & Sons)

Wells, D. C., Greisen, E. W., & Harten, R. H. 1981, A&AS, 44, 363

Werner, M. W., Roellig, T. L., Low, F. J., et al. 2004, ApJS, 154, 1, doi: 10.1086/422992

Yasuda, N., Fukugita, M., Narayanan, V. K., et al. 2001, AJ, 122, 1104, doi: 10.1086/322093

APPENDIX

A. PSF MATCHING

One needs to match PSFs of the images from various facilities before performing any pixel-to-pixel analysis. A Python script[16] for modeling PSFs in the SDSS and *Spitzer* mosaics was written to perform the PSF matching. First, SExtractor was run on each mosaic to generate a background image, as well as a catalog of sources. These sources were then used as the input values of the PyRAF DAOPHOT package (Stetson 1987). Stars having SExtractor parameter values listed below were selected and used to model the image PSF with the PyRAF task PSF:

- FLAGS $= 0$
- CLASS_STAR > 0.8 (0.7 for *Spitzer*)
- ELLIPTICITY < 0.1
- mode(FWHM_IMAGE) $-\,\sigma$(FWHM_IMAGE) $<$ FWHM_IMAGE $<$ mode(FWHM_IMAGE) $+\,\sigma$(FWHM_IMAGE).

A radius of 30 pixels was used for the PSF model, which was large enough to sample the wings of the PSF and small enough to exclude background objects. The generated PSF model was then fed into the task SUBSTAR, which subtracts any stars neighboring the PSF from the stars used to create the PSF-model. This cleans out the background and models the PSF to a higher degree of accuracy. This procedure was repeated one more time to finalize the modeling of each PSF.

PSF models of the *Spitzer* mosaics were consistent in shape, but with varying position angles (PAs). The PSF models were rotated to match the PAs, and then stacked to build a master PSF for the *Spitzer* mosaics. Before matching the PSFs of the SDSS mosaics, the PSFs needed to be rotated back to the original PA. The SDSS PSF model was constructed separately for each mosaic.

The PyRAF task PSFMATCH was used to match the PSFs of the SDSS g and r mosaics to *Spitzer* 3.6 μm mosaics. PSFMATCH convolved the input mosaics using a convolution kernel $k = \mathscr{F}[R/I]$, where $\mathscr{F}$ is the Fourier transform, R is the Fourier transform of the reference PSF (3.6 μm), and I is the Fourier transform of the input PSF (SDSS g or r band) (Phillips & Davis 1995). Nearly identical results were found regardless of the order that the tasks WREGISTER, PSF, and PSFMATCH were performed in.

B. PETROSIAN HALF-LIGHT RADIUS

The half-light radius (HLR) was measured to normalize the radial profiles of the galaxies so that they could be compared to those from the literature.

GD15 collapsed the spectral cubes in the rest-frame window 5635$\pm$45 Å, which is near the central wavelength of the V filter (5448 Å, see the Table 7 of K17) and then measured the HLR. Their HLR values thus measured are close to the Petrosian half-light radius (R^P_{50}; Blanton et al. 2001; Yasuda et al. 2001) from the SDSS data archive (see González Delgado et al. 2014, Appendix A).

To be consistent, we followed the definition of the SDSS Petrosian half-light radius, R^P_{50}. A radial surface profile was first determined using the median values of circular annuli in a radius range from 1 pixel to the semi-major axis of the galaxy.

Next, the Petrosian radius, R^P, was calculated such that the flux within an annulus between $0.8R^P$ and $1.25R^P$ was less than 20% of the total flux within the radius R^P. The radius containing 50% of the flux within R^P was defined to be the Petrosian half-light radius, R^P_{50}. Figure 10 shows the comparison between our measurements and the SDSS data archive values of R^P_{50} in r ('petroR50_r') of 182 coordinate-matched galaxies in our sample. The values from the '*Galaxy*' catalog on SDSS SkyServer DR14[17] were queried using the coordinates of our galaxy sample with a 0.5′ search radius. Overall, the galaxies match, so the R^P_{50} in the V band was used for the normalization of the radius in Figure 6.

C. BULGE-TO-TOTAL LIGHT RATIO

GALFIT (version 3; Peng et al. 2002, 2010) was used to measure the bulge-to-total light ratios (B/T) of the sample galaxies. The segmentation map generated for the β_V analysis was used for the 'Bad pixel mask'. The 3.6 μm mosaics for each galaxy, the master PSF of the 3.6 μm mosaics, and the 'Bad pixel mask' were used as inputs for GALFIT. The 'Image region' and 'Size of the convolution box' were set to the same as the images shown in Figure Set 2), which is twice the semi-major axis (column 7 in Table 1).

Three components, the disk 'expdisk', the bulge 'devauc', and 'sky', were input to the fitting procedure to decompose the galaxy light into light from the disk, the bulge, and the background, respectively. When a bright central point source was found and the galaxy is known to have an embedded AGN (column 18 and 19 in Table 1), we allowed for an additional 'psf' component and excluded that in the calculation of the bulge-to-total light ratio.

The following were used as the initial guesses for the GALFIT parameters:

- 'position' = the physical pixel position converted from R.A. and Decl.
- 'Integrated magnitude' = the magnitude in V
- 'R_e' = one fifth of the semi-major axis
- 'b/a' = from Table 1,

[16] https://github.com/DuhoKim/PSFtractor

[17] https://skyserver.sdss.org/dr14/en/tools/crossid/crossid.aspx

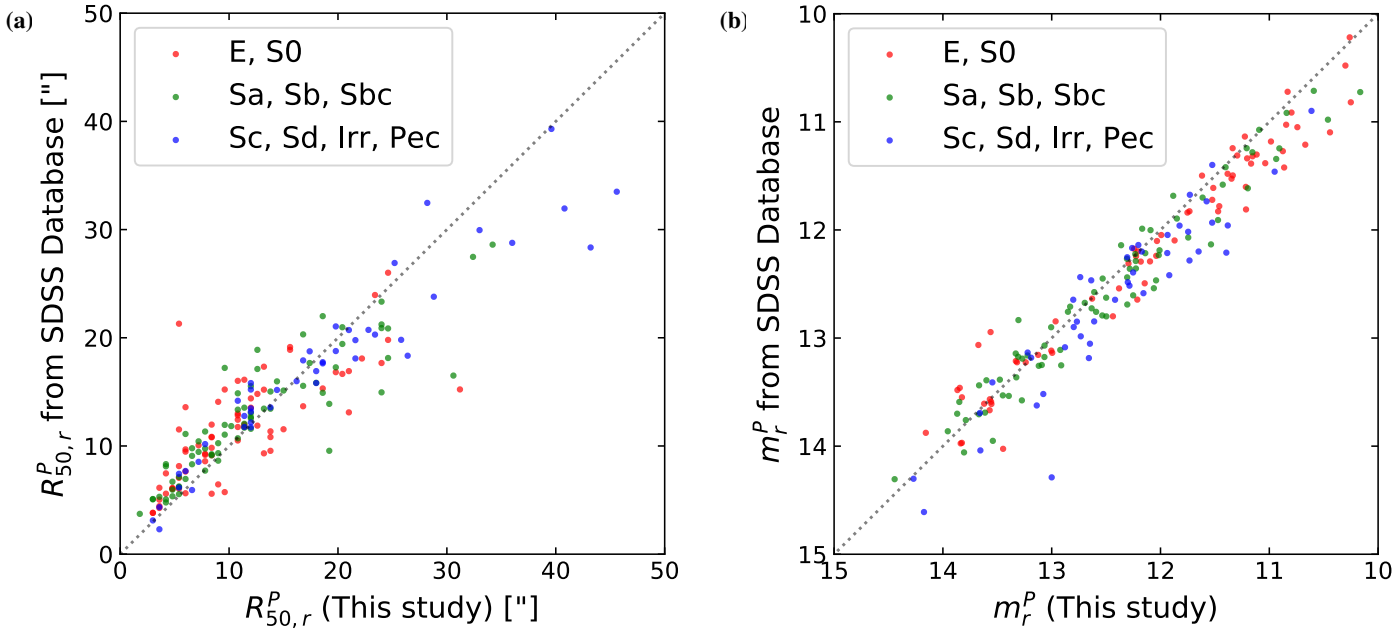

Figure 10. Comparison between (a) Petrosian half-light radii (*petroR50_r*) and (b) Petrosian magnitudes (*petroMag_r*) in r band from the catalog 'Galaxy' in the SDSS archive and our measurements using downloaded SDSS mosaics. The morphological types of galaxies are color coded. The almost one-to-one slope of our measurements and the SDSS measurements shows agreement with the archival catalog.

- 'PA' = from Table 1.

These parameters were then set as free, so they could be varied during the fitting process. We chose one fifth of the semi-major axis as the initial guess of the effective radius 'R_e'.

Upon visual inspection, any parameters that seemed unreasonable were fixed, and GALFIT was rerun. For the case when either the bulge or disk moved towards the outer part of the galaxy, the 'position' argument of GALFIT was set as fixed for both components. For the case where the bulge parameter, 'devauc', was seen to dominate the GALFIT fitting, a smaller effective radius, 'R_e', was forcefully set for the 'devauc' component to prevent unphysical fitting at large 'R_e'. This was seen to be the case for some late-type galaxies in the sample.

Figure 11 shows the "absolute magnitudes" (a) and the B/T (b) as a function of T-types in the RC3 catalog, excluding irregular and peculiar galaxies ($T \geq 9$). The 'Integrated magnitude' output from the GALFIT fitting for each of the 'expdisk' and 'devauc' components was converted from magnitudes to flux units. The summed flux values were converted back to the total magnitude of the entire galaxy. The distance modulus, which was determined from the redshift, was added to the total magnitude of the entire galaxy to determine the "absolute magnitude" for each galaxy. The reduced χ^2 value of each B/T fit is shown with different colors. The bulge component, 'devauc', dominates in the early-type galaxies ($T < 0$), while the disk component, 'expdisk', gradually increases with T-type. The B/T was used to subdivide the E–Sb galaxies in Figure 6, which show different shapes of A_V-profiles between this study and IFU-SED fitting method used in GD15. E, S0, Sa, and Sb galaxies were divided using boundary B/T values of $\simeq$ 0.7, 0.5, 0.45, and 0.25, respectively. Each group is shown in Figure 11 (b) with colored boxes for galaxies with larger (red) and smaller (blue) bulges than the dividing B/T values.

D. MASS-WEIGHTED METALLICITY

K17 published $\beta_{V,0}$-values for stellar populations having stochastic SFHs with metallicity evolutions taken into account. Figure 12 shows the specific SFRs (sSFRs), and the mass-weighted metallicity, $\langle Z \rangle_{\rm m}$, as a function of redshift. The gray solid, dashed, and dotted lines indicate amplitudes of multiple exponentially declining star-formation episodes for early-type (SFH3), spiral (SFH4), and late-type (SFH5) galaxies, respectively. The SFH3, SFH4, and SFH5 models are from Behroozi et al. (2013) for galaxies with stellar masses of $10^{11.4}$, $10^{10.95}$, and $10^{9.5}$ M$\odot$, respectively.

The $\langle Z \rangle_{\rm m}$ value is the sum of the products of SFR and metallicity divided by the sum of the SFRs up to a certain redshift ($z > $ x; see Equation 9 in K17). The colored solid, dashed, and dotted lines in Figure 12 are the $\langle Z \rangle_{\rm m}$ values of galaxies with SFH3, SFH4, and SFH5, respectively. K17 derived slopes for linear cosmic metallicity evolution as a function of redshift using the mass-metallicity relation from Maiolino et al. (2008) and three SFHs from Behroozi et al. (2013), which are -0.18 (SFH3), -0.03 (SFH4), and -0.58 (SFH5) (see also Fig.20 of Maiolino & Mannucci 2018). The orange, green, and blue lines represent different metallicity offsets, $Z(z = 0)$, of 2.5, 1.0, and 0.4 $Z\odot$, respectively. The lower limit of the metallicity evolution was selected as $Z = 0.0001$, which originated from the available SED models BC03 (Bruzual & Charlot 2003) and Starburst99 (Leitherer et al. 1999) that K17 used for young and old stellar populations. For example, the solid orange line represents the evo-

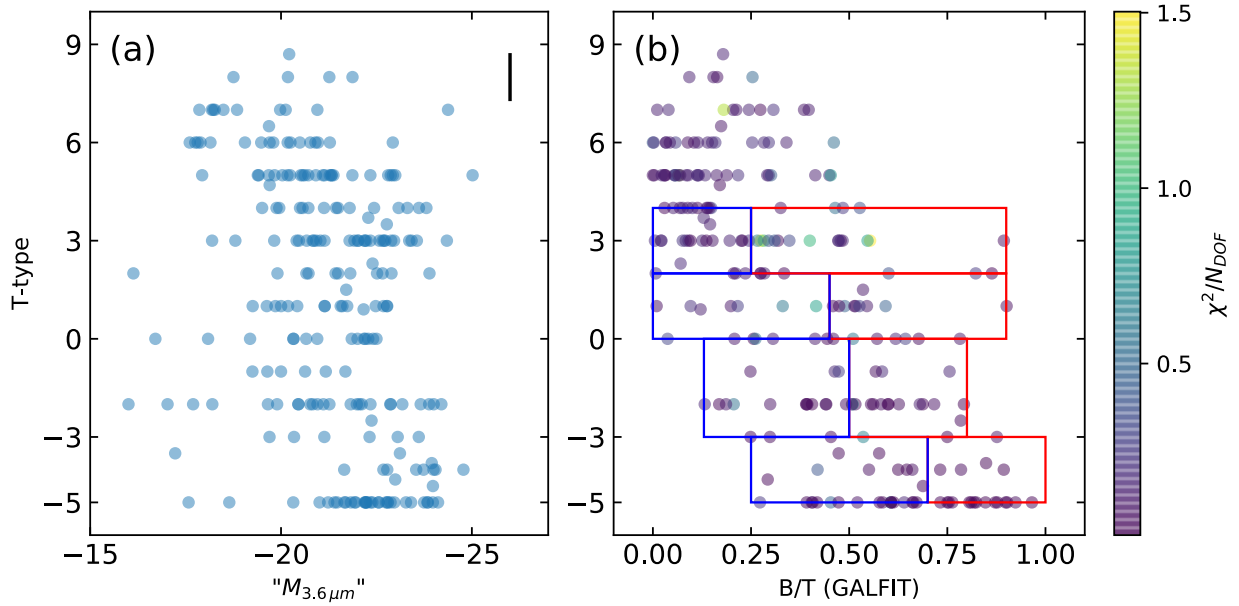

Figure 11. (a) RC3 T-type vs. total magnitude + distance modulus; (b) The bulge-to-total light ratios (B/T) measured using GALFIT versus RC3 T-type (excluding irregular and peculiar galaxies) of 239 galaxies. The colors of the dots in (b) represent the χ^2 divided by the number of pixels. The red (blue) boxes contain galaxies whose B/T values higher (lower) than 0.7, 0.5, 0.45, and 0.25 for E, S0, Sa, and Sb type galaxies, respectively, which consists of the 'Large bulge' (red) and 'Small bulge' (blue) subgroups for each Hubble types in Figure 7.

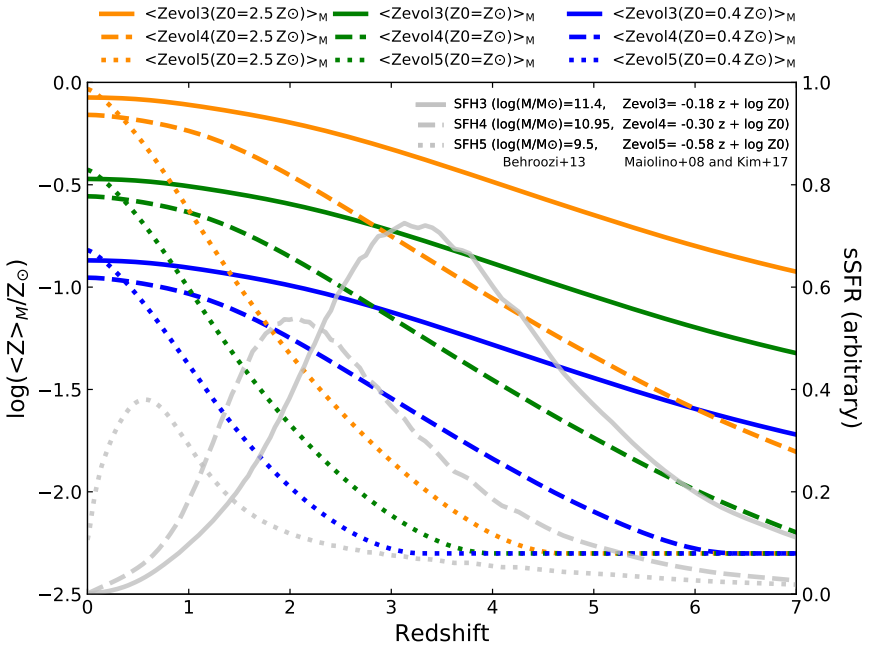

Figure 12. The mass-weighted metallicities, $\langle Z\rangle_{\rm m}$, and specific SFRs (sSFRs) as a function of redshift from K17 are indicated by the colored and gray lines, respectively. For sSFRs, K17 adopted SFRs of galaxies with stellar masses of $10^{11.4}$ (SFH3), $10^{10.95}$ (SFH4), and $10^{9.5}$ M$\odot$ (SFH5) from Behroozi et al. (2013). Linear metallicity evolution as a function of redshift was derived by K17 from these SFRs and the mass-metallicity relation of Maiolino et al. (2008). The $\langle Z\rangle_{\rm m}$ at a certain redshift, z_c, is the sum of the product of metallicity and SFR divided by the sum of the SFRs in the redshift range $z > z_c$. The lower metallicity limit at $\log Z/Z\odot \cong -2.3$ was set by the lowest metallicity available from SED models of simple stellar populations from BC03 and Starburst99 (for details, see Kim et al. 2017).

lution of the $\langle Z \rangle_{\rm m}$ of a galaxy having SFH3 with a slope of the linear metallicity evolution of -0.18 (Zevol3) with a metallicity offset, $Z(z=0)$, of $2.5\,Z\odot$. Due to massive galaxies having high metallicities and dwarf galaxies having low metallicities on average, Figure 12 would not show many galaxies with dotted orange or solid blue lines. Nonetheless, K17 showed all these results for completeness.

Nine $\langle Z \rangle_{\rm m}$ values at $z=0$ are shown in Figure 9 either above or below each colored line with the same color and line type as the corresponding colored lines in Figure 12.

E. β_V VS. AXIS RATIO

To avoid potential systematic uncertainties originating from a wide range of optical depths through edge-on galactic disks, we selected only face-on galaxies having axis-ratios (b/a) larger than 0.5. Figure 13 shows the relationship between β_V-values and their axis-ratio values. No significant correlation between β_V and the axis-ratio was seen in our sample to within the 1-σ errors (blue shaded regions). Sbc, Sd, and Irr&Pec types may show at best a hint of a positive correlation, although this is not significant within the current uncertainties.

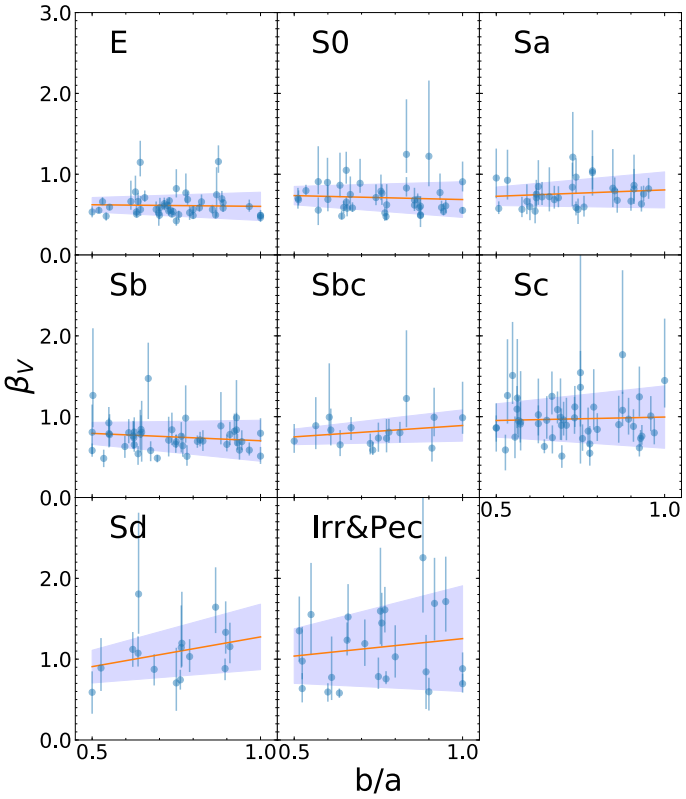

Figure 13. β_V versus b/a of individual galaxies for each in morphological type bin. Galaxies with $b/a < 0.5$ are not included in our sample. The best-fit regression is overlaid as orange lines, while the shaded region represents the ± 1-σ range. Only Sbc, Sd, and Irr&Pec galaxies in our sample show hints of a correlation between the β_V-value and the axis ratio for our sample. However, within the uncertainties this correlation does not seem to be statistically significant.